Universiteit Antwerpen

This item is the archived peer-reviewed author-version of:

Nanosecond pulsed discharge for CO_2 conversion : kinetic modeling to elucidate the chemistry and improve the performance

Reference:

Heijkers Stijn, Martini Luca Matteo, Dilecce Giorgio, Tosi Paolo, Bogaerts Annemie.- Nanosecond pulsed discharge for CO_2 conversion : kinetic modeling to elucidate the chemistry and improve the performance

The journal of physical chemistry: C : nanomaterials and interfaces - ISSN 1932-7447 - 123:19(2019), p. 12104-12116

Full text (Publisher's DOI): https://doi.org/10.1021/ACS.JPCC.9B01543

To cite this reference: https://hdl.handle.net/10067/1599760151162165141

uantwerpen.be

Institutional repository IRUA

Nanosecond Pulsed Discharge for CO_2 Conversion: Kinetic Modelling to Elucidate the Chemistry and Improve the Performance

Stijn Heijkers[1] , Luca Matteo Martini[2†], Giorgio Dilecce[2,3], Paolo Tosi[2,3] and Annemie Bogaerts[1*]

[1] Research group PLASMANT, Department of Chemistry, University of Antwerp, Universiteitsplein 1, BE-2610 Wilrijk-Antwerp, Belgium

*annemie.bogaerts@uantwerpen.be, +3232652377

[2] Dipartimento di Fisica, Università di Trento, Italy

[3] P.Las.Mi Lab NANOTEC – CNR Bari, Italy

[†] Present address: Department of Applied Physics, Eindhoven University of Technology, The Netherlands

Abstract

We study the mechanisms of CO_2 conversion in a nanosecond repetitively pulsed (NRP) discharge, by means of a chemical kinetics model. The calculated conversions and energy efficiencies are in reasonable agreement with experimental results over a wide range of specific energy input (SEI) values, and the same applies to the evolution of gas temperature and CO_2 conversion as a function of time in the afterglow, indicating that our model provides a realistic picture of the underlying mechanisms in the NRP discharge, and can be used to identify its limitations, and thus, to suggest further improvements. Our model predicts that vibrational excitation is very important in the NRP discharge, explaining why this type of plasma yields energy efficient CO_2 conversion. A significant part of the CO_2 dissociation occurs by electronic excitation from the lower vibrational levels towards repulsive electronic

states, thus resulting in dissociation. However, vibration-translation (VT) relaxation (depopulating the higher vibrational levels) and CO+O recombination ($CO + O + M \rightarrow CO_2 + M$), as well as mixing of the converted gas with fresh gas entering the plasma in between the pulses, are limiting factors for the conversion and energy efficiency. Our model predicts that extra cooling, slowing down the rate of VT relaxation and of the above recombination reaction, thus enhancing the contribution of the highest vibrational levels to the overall CO_2 dissociation, can further improve the performance of the NRP for energy efficient CO_2 conversion.

1. Introduction

The atmospheric CO_2 concentration has been increasing from approximately 270 ppm to values exceeding 400 ppm during the last centuries, inducing accelerated climate change [1]. A large reduction of greenhouse gas emissions is therefore needed to keep the increase in global average temperature well below 2°C, as agreed at the Paris climate conference (COP21) [2]. Technologies for converting CO_2 into value-added products are therefore highly needed, as they can turn waste back into new feedstock, following the cradle-to-cradle principle [3].

In recent years it has been shown that plasma technology can be a suitable candidate for CO_2 conversion [4,5]. Not only pure CO_2 splitting into CO and O_2 [6–15], but also mixtures with CH_4 [16–24] (i.e., dry reforming of methane), H_2O [25], N_2 [26,27] and H_2 [28] are being studied. The most common plasma reactors used for this purpose are dielectric barrier discharges (DBDs), microwave (MW) plasmas and gliding arc (GA) discharges. However, other plasma reactors are also being investigated, and seem quite promising, such as atmospheric pressure glow discharges, spark discharges, and nanosecond repetitively pulsed (NRP) discharges [4].

NRP discharges exhibit conversions up to 45%, with energy conversion efficiencies up to 60% for dry reforming[29], and CO_2 conversions of 10-20% with energy efficiencies of

12-30% for pure CO_2 splitting [30]. It is suggested that this type of discharge shows a high degree of non-equilibrium, explaining these high conversions and energy efficiencies [29,30]. Detailed diagnostics experiments in pure CO_2 and CO_2/H_2O mixtures have recently been performed [30,31], but to our knowledge, no chemical kinetics model has been developed yet, to support the experiments, and to obtain additional insight in the underlying mechanisms, responsible for the high conversions and energy efficiencies. Such a model could be helpful to further improve the performance of NRPs for energy efficient CO_2 conversion.

Therefore, in this paper we present a detailed study of the CO_2 conversion in an NRP discharge, using 0D chemical kinetics modelling, validated by experiments. We have to make quite some assumptions in the 0D model, in order to account for the characteristic features of the NRP discharge, which will be explained in the next section. However, as we want to study the detailed chemistry, including the role of the vibrational kinetics, many different species (and excited levels) must be included in the model, which would lead to excessive calculation times in a more-dimensional model. Therefore, a 0D model is the most appropriate (and currently the only feasible) model to describe the detailed reaction kinetics. This model allows us to elucidate the most important CO_2 dissociation mechanisms, pointing towards the role of vibration induced dissociation in energy-efficient CO_2 conversion. Furthermore, our model can also pinpoint the limitations, and therefore suggest further improvements for the experiments, as will also be demonstrated.

2. Model description

First, we will give a brief description of the 0D model and the chemistry used to describe CO_2 splitting, followed by explaining the assumptions made in the 0D approach to describe the NRP discharge.

2.1 0D Model equations and chemistry

The 0D model is based on solving the conservation equations (1) for all species included in the model (see below):

$$\frac{\partial n_s}{\partial t} = \sum_{i=1}^{j}[(a_{s,i}^{R} - a_{s,i}^{L})R_i] \quad (1)$$

where n_s is the density of species s (in cm^{-3}) , j the total number of reactions, $a_{s,i}^{L}$ and $a_{s,i}^{R}$ the stoichiometric coefficients at the left hand side and right hand side of the reaction and R_i the rate of reaction (in cm^{-3} s^{-1}), given by:

$$R_i = k_i \prod_s n_s^{a_{s,i}} \quad (2)$$

where k_i is the rate constant (in cm^3 s^{-1} or cm^6 s^{-1} for two-body or three-body reactions, respectively) and $a_{s,i}$ was defined above.

The chemistry set used in this study is based on the original model of Kozák et al., [32] which was further evaluated by Berthelot et al. [33]. It contains 58 different species (see Table 1), i.e., four ground state molecules, three radicals, 11 ions, the electrons, and 39 excited species, including the 21 vibrational levels of the asymmetric stretch mode up to the dissociation limit. These species react with each other, by means of electron impact reactions, electron-ion recombination reactions, ion-ion, ion-neutral and neutral-neutral reactions, as well as vibration-translation (VT) and vibration-vibration (VV) relaxation reactions. The electron impact reaction rate constants are calculated using a pre-evaluated electron energy distribution function (EEDF; which is regularly updated during the simulations based on the new chemical composition in the plasma) and the cross section set of Phelps with the 7 eV threshold excitation reaction used for dissociation [34–36] as suggested by Grovulovic´ et al. [37], Bogaerts et al. [38] and Pietanza et al. [39–41]. More information about the model and the chemistry set can be found in the Supporting Information (SI).

Table 1: Species taken into account in the 0D model (the symbols (V) and (E) stand for the vibrational and electronically excited levels, respectively).

Molecules	Charged species	Radicals	Excited species
CO_2, CO	CO_2^+, CO_4^+, CO^+, C_2^+, C^+, CO_3^-, CO_4^-	C	CO_2(Va, Vb, Vc, Vd), CO_2(V1-V21), CO_2(E1), CO(V1-V10)
O_2, O_3	O^+, O_2^+, O^-, O_2^-	O	O_2(V1-V4)
	Electrons		

2.2 Modelling the NRP discharge with a 0D approach

The NRP discharge under study is based on the experimental design used by Martini et al. [30], schematically illustrated in Figure 1. The discharge is maintained in a pin-to-sphere configuration. The high-voltage (HV) pin electrode is a narrow tube with an external diameter of 1.65 mm, and an internal diameter of 1.2 mm, through which the inlet gas flows. The grounded electrode is a stainless steel sphere with 8 mm diameter, containing the outlet. The interelectrode distance is 5 mm. The electrodes assembly is contained in a vacuum tight chamber made of a 35 mm diameter glass tube, in which a pressure equal to atmospheric pressure is maintained. The gas flows from the HV anode at a rate of 100 sccm, flows around the cathode and exits the chamber through two 2 mm diameter apertures about 30 mm downstream the cathode. The pulse is triangular with a duration of 10 ns (FWHM) and the pulse energy is varied between 7.2 mJ and 13.8 mJ. This corresponds to average powers ranging from 0.72 MW till 1.38 MW and maximum powers inside the pulse ranging from 1.44 MW till 2.76 MW. Finally, the pulse frequency is varied between 600 Hz and 3 kHz.

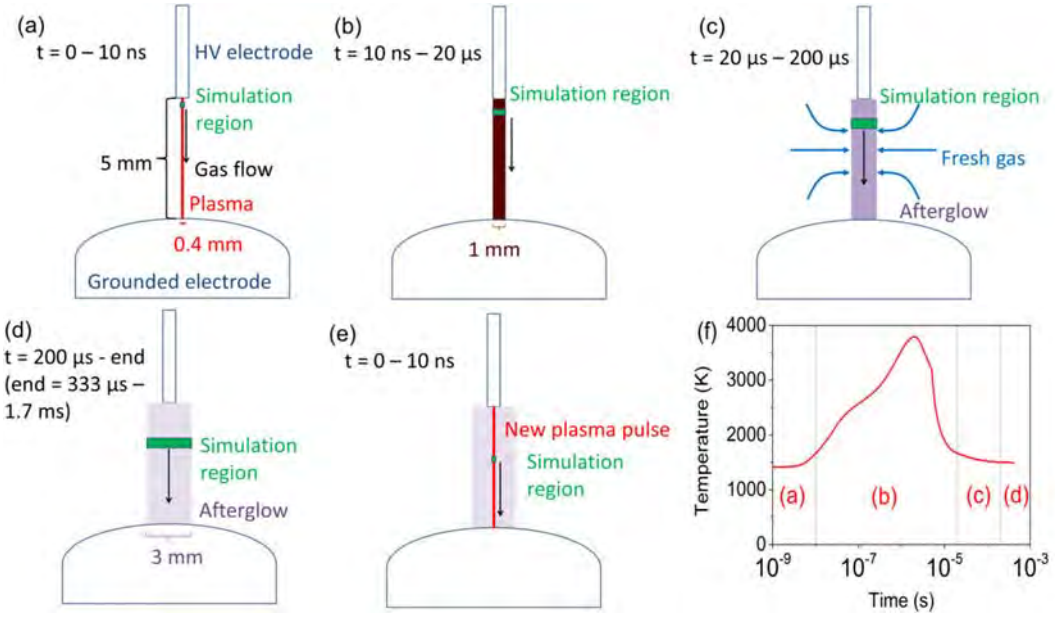

Figure 1: Schematic illustration of the reactor setup, described in the 0D model, during the pulse (a), at the end and right after the pulse when most heating takes place (b), in the afterglow when new gas enters the plasma region till 200 µs after the pulse (c), and before the next pulse starts (d). Finally, the cycle begins again for subsequent pulses, where the new plasma is surrounded by partially converted CO_2 gas (e). The red area represents the plasma, the black-grey zone indicates the afterglow (with a darker color yielding a higher temperature). An example of the temperature evolution of one pulse and afterglow is given in panel (f) for an intermediate specific energy input (SEI) of 2.6 eV molec^{-1}. In general, the maximum temperature varies between 2550 K and 4150 K, while it is between 660 K and 1756 K after cooling down in the afterglow, for SEI values ranging between 0.7 eV molec^{-1} and 4.7 eV molec^{-1}. It takes minimum 7 pulses (for SEI= 0.7 eV molec^{-1} and frequency of 600 Hz) and maximum 14 pulses (for SEI=3.0 eV molec^{-1} and frequency of 3 kHz) for CO_2 molecules to travel from HV electrode to grounded electrode.

Modelling the NRP discharge with a 0D model is quite challenging, because the plasma volume rises during the pulse and afterglow, and the surrounding gas can enter the plasma volume (see Figure 1), and these effects are not automatically captured in a 0D model. Therefore, we had to make the following assumptions:

- We assume the plasma region to be initially a cylinder with 5 mm length, i.e. the interelectrode distance, and an initial diameter of 0.4 mm, which is the characteristic diameter of a streamer in air [5]. A similar value (0.35 mm) was also measured by

Stancu et al. [42] in a similar configuration for an interelectrode distance of 4 mm and a pulse duration of 10 ns in air, albeit for a maximum power of 0.1 MW per pulse, which is about ten times lower than the typical powers used in the NRP discharge under study here [30] . More recently, Castela et al. mentioned a diameter of 0.45 mm [43] for an interelectrode distance of 1 mm and an energy per pulse (τ=20 ns) of 1.4-1.5 mJ in a lean methane-air mixture, which corresponds to a maximum power of 0.07 - 0.075 MW per pulse. Furthermore, Lo et al. [44], reported a discharge diameter after the pulse of approximately 1 mm, using an energy of 20 mJ per pulse with 20 ns pulse duration, corresponding to a power of 1 MW, for a discharge gap of 6.5 mm in air. The latter configuration is closest to the one under study here. Finally, the discharge diameter has also been used in modelling work by Popov [45], who assumed a value of 1 mm as well. Therefore, during the pulse, we let the plasma volume increase, by increasing the diameter from 0.4 mm till 1 mm (panel (a) and (b) in Figure 1). This determines the plasma volume, i.e., the volume in which the power is deposited (i.e., rising from 0.6 mm^3 at the start, until 3.9 mm^3 at the end of the pulse).

- In between pulses, no power is deposited, but chemical reactions can still take place in this "afterglow" region, due to the high temperature and reactive species present. The diameter of the afterglow region does not stay constant either, as shown by Castela et al. [43]. We assume a constant diameter of 1 mm until 20 µs after the pulse, as demonstrated by calculations of Castela et al. [43]. After 20 µs, the diameter increases to 2.4 mm at 138 µs and to 3 mm at 200 µs (panel (c) and (d) in Figure 1). This means that extra gas enters the afterglow region. The final diameter of 3 mm is held constant during the rest of the interpulse time, based on the experimental data in [43]. When a new pulse starts, the diameter of the plasma volume is again set to 0.4 mm (panel (e)), repeating the above cycle for all pulses. However, starting from the second pulse, the

fresh gas in the afterglow is not pure CO_2 anymore, but has a gas composition adopted from the end of the afterglow of the previous pulse (as schematically illustrated in panel (e) of Figure 1).

- The gas temperature is calculated self-consistently in the same manner as done by Kozak et al. [46] with a more detailed explanation given in the SI. Generally, the temperature increases slightly inside the pulse with a large rise just after the pulse, as illustrated in panel (f) in Figure 1, and experimentally measured by Martini et al. [30]. From then on, due to gas expansion and dilution of the plasma mixture, the temperature in the afterglow drops (see also panel (f) in Figure 1) until the next pulse is reached.
- We assume the temperature of the fresh gas entering the afterglow region (upon rising of this volume from 20 μs up to 200 μs; see panel (c) in Figure 1) to be equal to the average of the temperature inside the afterglow (i.e., ranging between 2550 K and 4150 K) and the temperature of the surrounding gas, based on Castela et al. [43] and Lo et al. [44]. The surrounding gas is initially at room temperature in the first pulse, while for the subsequent pulses, we assume it to be equal to the temperature in the afterglow region just before the new pulse starts (i.e., ranging between 660K-1756 K).
- In addition, gas expansion occurs upon conversion of CO_2 into CO and ½ O_2, so we calculate the gas pressure and mass flow rate at every time step from the actual species densities, gas temperature and velocity. The species densities (as calculated with the conservation equations; see equation (1) above) and velocity are then corrected to account for this effect and to maintain a constant (atmospheric) pressure and mass flow rate, following the method of Kozak et al. [46] This gas expansion is initiated at 5 μs after the pulse, which is the typical time when this effect becomes visible [47]. It is crucial to include this, as also stated by Pinhaõ et al. [48] , to avoid

systematic errors in computing process parameters in plug flow-like reactors. Indeed, serious speeding up of the gas after the pulse due to gas heating and conversion, as observed by Seydou et al. [49], would otherwise not be included and therefore the residence time and thus conversion could be largely overestimated.

The CO_2 conversion, X_{CO_2} , is defined as:

$$X_{CO_2}(\%) = 100\% \left(1 - \frac{n_{CO_2,e}\, v_e}{n_{CO_2,i}\, v_i}\right) \quad (3)$$

where $n_{CO_2,e}$ and v_e are the CO_2 density and gas velocity at the end of the plasma region near the grounded electrode, and $n_{CO_2,i}$ and v_i are the CO_2 density at room temperature and gas velocity at the inlet (pin electrode), i.e., 25.3 cm s^{-1}.

To evaluate the effect of our choice of initial plasma volume and of the volume expansion during the pulse and afterglow on the calculation results, we plot in figure 2 the calculated CO_2 conversion as a function of specific energy input (SEI), for different assumed values of initial plasma diameter (figure 2(a)) and final afterglow diameter (figure 2(b)). Upon increasing the initial plasma diameter, the CO_2 conversions drops, as expected, due to the lower power density deposited inside the pulses. In addition, a larger final afterglow diameter also yields a lower CO_2 conversion, despite the fact that it corresponds to a longer residence time and thus more deposited pulses for the same flow rate (see below). The reason is of course the more pronounced dilution of the afterglow volume with untreated CO_2 gas. The dip at 2.3 eV $molec^{-1}$ at larger final afterglow diameters can be explained by the smaller number of pulses deposited(defined by the frequency, and thus the time between pulses, which varies for the different SEI values; see also further in the text)

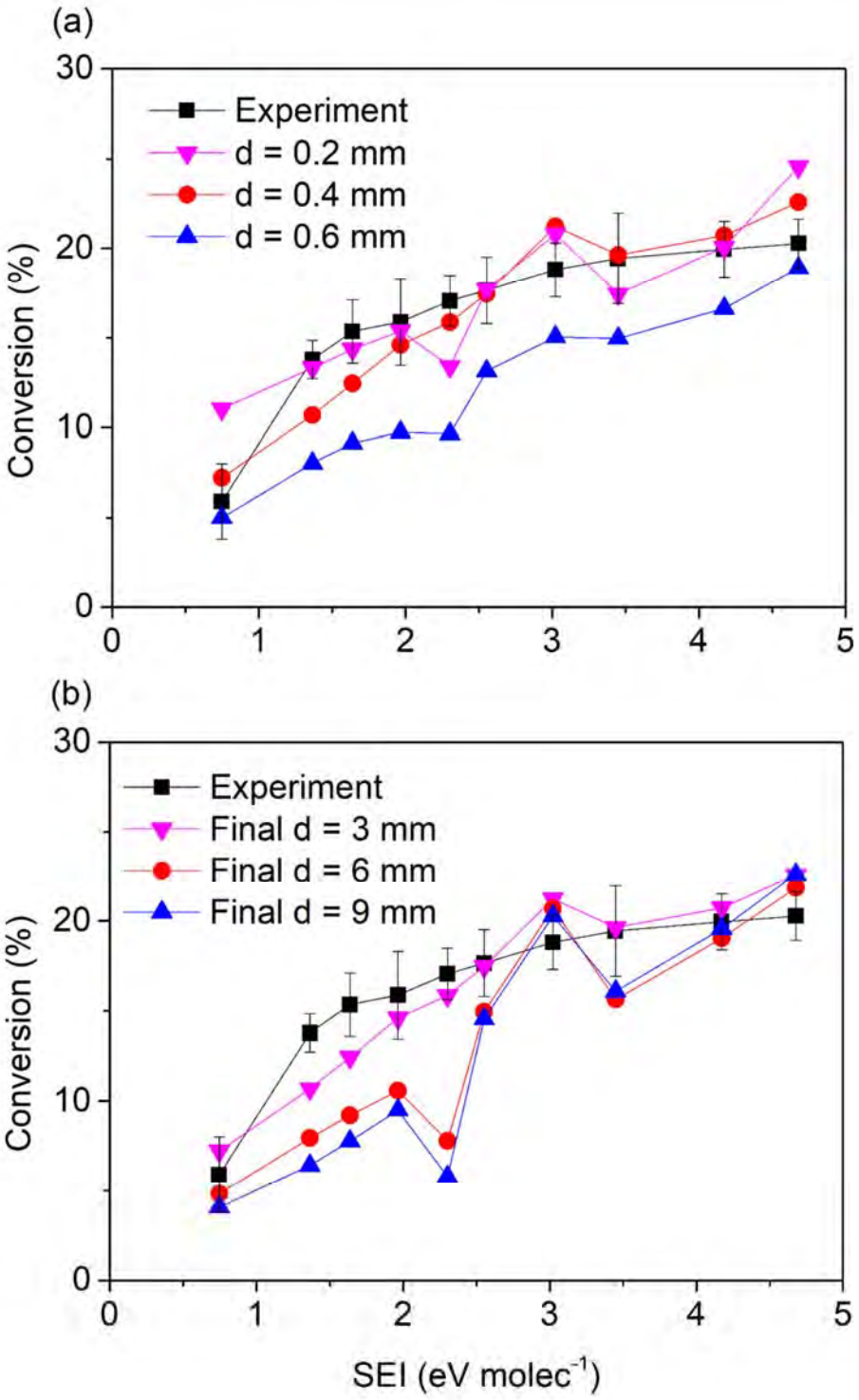

Figure 2: Experimental and calculated CO_2 conversions as a function of SEI, for different initial plasma diameters, and a final afterglow diameter of 3 mm (a), and for different final

afterglow diameters at an initial plasma diameter of 0.4 mm (b), to evaluate the effect of the choice of these parameters on the calculated CO_2 conversion. In our model, we use an initial plasma diameter of 0.4 mm and a final plasma diameter of 3 mm (see above).

This inlet gas velocity would correspond to a gas residence time of about 20 ms. However, gas expansion due to conversion and gas heating greatly enhance the gas velocity and thus reduce the residence time, resulting in residence times ranging between 11.7 ms at SEI = 0.7 eV molec^{-1} and 4.3 ms at SEI = 4.7 eV molec^{-1}. Together with the fact that the pulse duration is 10 ns, while the afterglow time varies from 333 µs to 1.7 ms (depending on the exact power deposition and frequency used; see SI) , these gas residence times correspond to 7-14 pulses (and corresponding afterglows), again depending on the exact power deposition and frequency used (see detailed explanation in the SI). The smallest number of pulses (i.e. 7) is at SEI = 0.7 eV molec^{-1} where the lowest frequency is used, i.e. 600 Hz. The largest number of pulses (i.e. 14) is at SEI = 3.0 eV molec^{-1} where the highest frequency is used, i.e. 3 kHz. This frequency is also applied at the highest SEI value studied, i.e. 4.7 eV molec^{-1}, but due to the higher power deposition, gas heating and gas expansion are higher in this case, so that the residence time is lower, and the molecules thus experience a lower number of pulses than at SEI = 3.0 eV molec^{-1}. The maximum velocity obtained at SEI = 4.7 eV molec^{-1} is 596 cm s^{-1}, while at SEI = 0.7 eV molec^{-1}, it is 293 cm s^{-1}. Seydou et al. [49] measured a similar steady-state gas velocity of 370 cm s^{-1} after the pulse, for a pulse energy of approximately 1 mJ and a frequency of 30 kHz in methane-air-N_2 mixtures.

The number of pulses experienced by the gas molecules when travelling from HV electrode to grounded electrode is schematically illustrated in figure 3, for the case of the smallest and largest number of pulses.

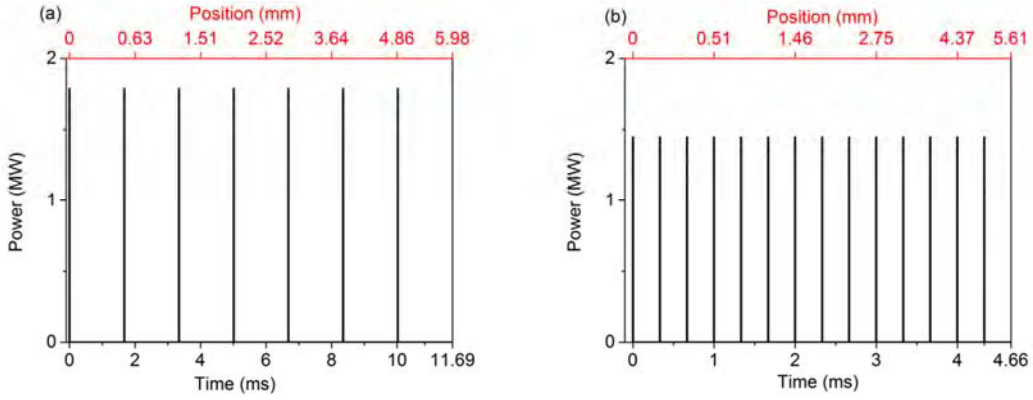

Figure 3: Power deposition in subsequent pulses as a function of time and position, at SEI = 0.7 eV molec^{-1} with frequency of 600 Hz, yielding the smallest number of pulses (i.e. 7) (a), and at SEI = 3.0 eV molec^{-1} with frequency of 3 kHz, yielding the largest number of pulses (i.e. 14) (b). Note that the position axis is non-linear due to gas expansion, which speeds up the gas and is most pronounced in the case of SEI = 3.0 eV molec^{-1}. The time axis stops at the residence time for that particular condition.

After each pulse, between 20 µs and 200 µs, gas mixing is introduced in every time step, by diluting the afterglow mixture, using:

$$n_{s,new} = \frac{n_{s,old}\, r_{old}^2 + \omega_s N_{gas}(r_{new}^2 - r_{old}^2)}{r_{new}^2} \quad (4)$$

for each species s, where $n_{s,new}$ and $n_{s,old}$ are the species number densities after and before dilution, r_{new} and r_{old} are the radii of the afterglow volume at the current and previous timestep, respectively, ω_s is the fraction of species s in the fresh incoming gas and N_{gas} the total gas density, calculated by the ideal gas law.

In the afterglow of the first pulse, the incoming gas is pure CO_2. For the other pulses, it is equal to the gas composition obtained at the end of the afterglow of the previous pulse, as explained above, because some of the CO_2 has already been converted into CO, O and O_2. If this gas mixing (due to fluid dynamics) would not be included and the plasma composition

would only depend on the chemical kinetics, the calculated conversion at the lowest SEI studied (0.7 eV molec^{-1}) would be already 20 % after one pulse. It is thus necessary to include the effect of gas mixing, even in an approximate way.

The SEI is originally calculated as [30]:

$$SEI(kJ\ L^{-1}) = \frac{P_d(W)}{\Phi(cm^3 s^{-1})} = \frac{\widetilde{E_p}(J) f_p(Hz)}{\Phi(cm^3 s^{-1})} \quad (5)$$

in which P_d is the overall power deposited to the NRP discharge, ranging from 5.34 W till 33.6 W (based on the combinations given in Table 2, which are also the experimental conditions from Martini et al. [30]), $\widetilde{E_p}$ the average discharge pulse energy, ranging from 7.2 mJ till 13.8 mJ, f_p the pulse repetition frequency, ranging from 600 Hz till 3 kHz, and Φ the gas flow rate, taken constant at 100 sccm or 1.67 cm^3 s^{-1}. Since it is more convenient to express this unit in eV molec^{-1} (see equation 7) to better assess the energy efficiency, the SEI can also be calculated as:

$$SEI(eV\ molec^{-1}) = \frac{SEI(kJ\ L^{-1})\ 22.4(L\ mol^{-1})\ 6.242x10^{21}(eV\ kJ^{-1})}{6.022x10^{23}(molec\ mol^{-1})} \quad (6)$$

The combinations of average discharge pulse energy and frequency used in this study (see Table 2) correspond to the above mentioned overall power deposition range, and thus to SEI values ranging between 3.2 kJ L^{-1} and 20.2 kJ L^{-1}, or between 0.7 eV molec^{-1} and 4.7 eV molec^{-1}. The exact energy deposited per pulse, applied frequency, and the corresponding number of pulses deposited (accounting for gas expansion), are plotted for each SEI value investigated in Figure S.1 of the SI. Using these quantities, the energy efficiency η (in %) and the energy cost (EC) (in eV molec^{-1}) can be calculated:

$$\eta(\%) = \frac{X_{CO_2}(\%)\ \Delta H_{CO_2}(eV\ molec^{-1})}{SEI\ (eV\ molec^{-1})} \quad (7)$$

$$EC(eV\ molec^{-1}) = \frac{SEI(eV\ molec^{-1})}{X_{CO_2}(\%)/100} \quad (8)$$

where ΔH_{CO_2} is the energy cost to split one CO_2 molecule in CO and ½ O_2, i.e. 2.9 eV molec^{-1}.

Table 2: Conditions studied in the simulations and in the experiments from Martini et al. [30]

SEI (kJ L^{-1})	**SEI (eV molec^{-1})**	**Average energy per pulse (mJ)**	**Frequency (kHz)**	**Interpulse time (µs)**	**Overall power deposited, P_d (W)**
3.2	0.7	8.9	0.6	1700	5.34
5.9	1.4	8.2	1.2	833	9.84
7.1	1.6	7.9	1.5	667	11.85
8.5	2.0	7.9	1.8	556	14.22
9.9	2.3	13.8	1.2	833	16.56
11.0	2.6	7.6	2.4	417	18.24
13.0	3.0	7.2	3	333	21.60
14.9	3.4	10.3	2.4	417	24.72
18.0	4.2	11.1	2.7	370	29.97
20.2	4.7	11.2	3	333	33.60

3. Results and Discussion

3.1. Validation of the model and overall plasma characteristics

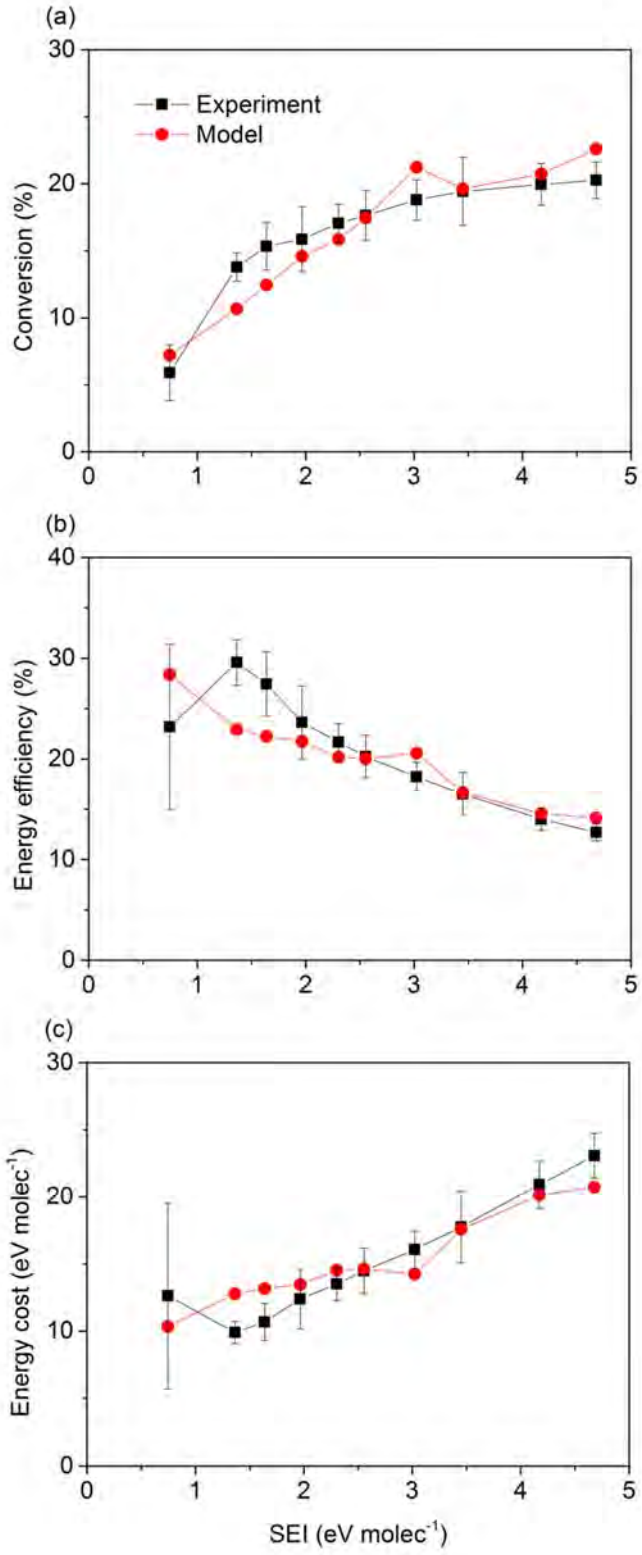

Figure 4: Calculated and experimental CO_2 conversion (a), energy efficiency (b) and energy cost (c), as a function of SEI.

To validate the model, the CO_2 conversion, energy efficiency and energy cost obtained at the end of the simulation, corresponding to the overall values obtained in experiments, are compared with the experimental data from Martini et al. [30], and they are plotted as a function of SEI in Figure 4. Moreover, in Figure 5 (a,b), we compare the evolution of the calculated gas temperature and conversion in the afterglow as a function of time with the experiments[30]. The conditions here are slightly different from those in Table 2, i.e., SEI = 1.7 eV molec^{-1} , corresponding to bursts of four pulses, separated by 333 µs (i.e. 3 kHz), followed by a pause of 3.33 ms before the next burst starts. The average discharge pulse energy is set to 10 mJ, yielding a total of 8 pulses. In this way, we are able to compare at the same conditions as in the experiments.

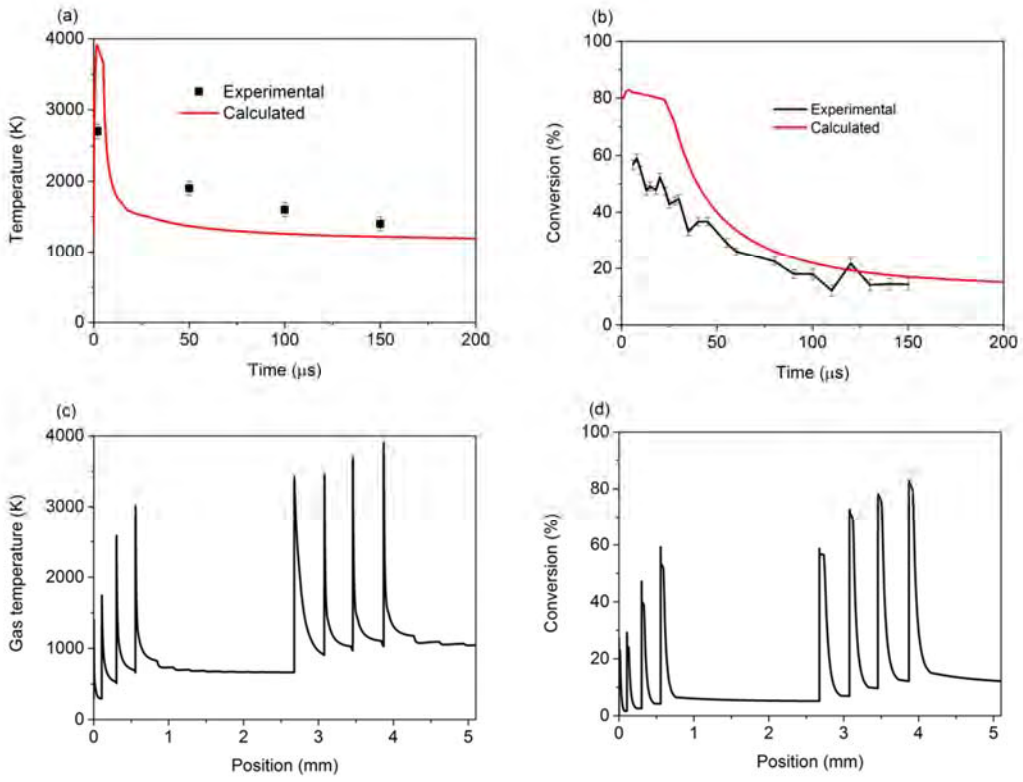

Figure 5: Evolution of temperature (a) and CO_2 conversion (b) as a function of time in the afterglow after the last pulse, in comparison with the experimental data of Martini et al. [30], and evolution of temperature (c) and CO_2 conversion (d) as a function of travelled distance between pin electrode and grounded electrode**,** all at SEI = 1.7 eV molec^{-1}. Note that the model applies to pure CO_2, while the experiments had to be carried out in the presence of 1.35% H_2O.

The calculated overall CO_2 conversion, energy efficiency and energy cost show satisfactory agreement with the experiments in the entire range of SEI values, with an average relative error of 11 % for the conversion, energy efficiency and energy cost; see Figure 4. At the lower SEI values, the largest discrepancies are found, with a maximum relative error of 25 % at SEI = 1.4 eV molec^{-1}. In addition, at SEI = 0.7 eV molec^{-1}, the trend in energy efficiency and energy cost seems not correctly reproduced, but the experimental error bars are quite large for this lowest SEI value. The reason for the larger discrepancy at the lower SEI values can be due to the fact that we slightly overestimated the diameter of the plasma region at the lower SEI values. Indeed, we assumed the same value for all SEI values in our simulations (cf. Figure 1), but lower pulse energies usually give rise to a smaller plasma volume,[47] yielding a somewhat higher power density, and thus, a somewhat larger conversion would have been achieved if we would have used a somewhat smaller diameter. However, in general, the agreement between simulations and experiments is quite reasonable.

The CO_2 conversion and gas temperature as a function of time in the afterglow, at SEI = 1.7 eV molec^{-1}, also shows satisfactory agreement with the experimental results, as can be seen in Figure 5 (a,b). It should be realized that the model applies to pure CO_2, while the experiments were carried out in the presence of 1.35% H_2O, which was needed to produce the OH that was used to measure the fragmentation kinetics of CO_2 by collisional energy transfer laser-induced fluorescence and to determine the gas temperature profile. While the presence of 1.35% H_2O might affect the gas temperature and CO_2 conversion to some extent, it will not be too critical for the purpose of this comparison.

The comparison is made for the afterglow of the last pulse, because the conversion and gas temperature do not change significantly anymore compared with the previous pulses

(i.e. maximum relative increase of 6 % per pulse for the temperature and 9 % for the conversion; see Figure 5(c,d)), so the system has more or less reached steady state conditions.

The conversion and gas temperature clearly drop in the afterglow, in both the model and experiments. In addition, although the conversion and gas temperature are overestimated right after the pulse, the absolute values show satisfactory agreement. The model indeed predicts extensive heating just after the pulse, yielding a significant temperature rise of about 2150 K right after the pulse for the particular SEI value of 1.7 eV molec^{-1} and 1400 K on average for all conditions studied. This heating is attributed to both recombination reactions and VT relaxation (see Figure 6). More specifically, three-body recombination ($CO + O + M \rightarrow CO_2 + M$) is an exothermic reaction, and VT relaxation transfers energy from the CO_2 vibrational levels into translational modes of freedom, so both processes give rise to gas heating. As is clear from Figure 6, they both contribute on average with 35 % to the overall gas heating. Note that at SEI = 2.3 eV molec^{-1} the relative importance of recombination is slightly higher than VT transfer, while the opposite is true for the other SEI values. This is because at this SEI value the energy deposited per pulse is higher (see Table 2, and Figure S.1(a) in SI). Indeed, the SEI does not only depend on the energy deposited per pulse, but also on the time in between pulses (defined by the frequency), which is larger for this SEI value, compared to the SEI values of 2.0 eV molec^{-1} and 2.6 eV molec^{-1} (cf. Table 2 above). Therefore, cooling in between pulses is more effective at SEI = 2.3 eV molec^{-1}, which results in a lower final temperature at the end of the afterglow (i.e. this temperature is 1289 K at SEI = 2.0 eV molec^{-1}, 1026 K at SEI = 2.3 eV molec^{-1}, and 1484 K at SEI = 2.6 eV molec^{-1}) and thus somewhat less VT relaxation, as demonstrated in Figure 6. This, however, has no visible effect on the CO_2 conversion (cf. Figure 4).

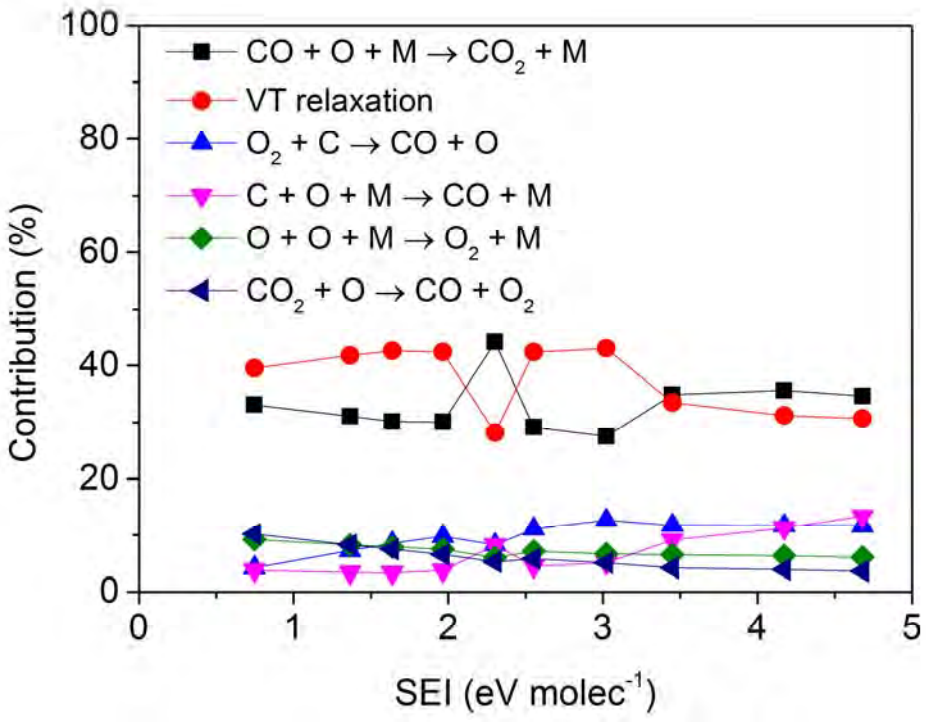

Figure 6: Contribution of the most important gas heating mechanisms after the pulse, as a function of SEI.

Figure 5 (b,d) also clearly demonstrates that the conversion drops from above 50% at the end of the pulse, till below 20% after 150 µs in the afterglow. This is both attributed to recombination reactions (forming again CO_2; see also section 3.2) and dilution of the converted gas mixture by fresh unreacted gas entering the plasma zone. Although a 0D model cannot capture all flow phenomena in an NRP discharge, the agreement with experiments is quite good, both for the conversion and gas temperature, so we can use the model to elucidate the chemistry occurring during the pulse and afterglow, which might help to further improve the overall performance of this type of plasma.

In Figure 7 we plot the calculated plasma characteristics, i.e., gas temperature (a), electron temperature (b), electron density (c), and CO_2 conversion (d), for the lowest and highest SEI values studied, i.e. SEI = 0.7 eV molec^{-1} and 4.7 eV molec^{-1}. The calculated plasma characteristics for the other SEI values lie in between these values, and are illustrated

in the SI for two intermediate SEI values (Figure S.2). The gas temperature becomes very high in the early afterglow, with values exceeding 2000 K for the lowest SEI value of 0.7 eV molec^{-1}, and even above 4000 K for the highest SEI of 4.7 eV molec^{-1}. Subsequently, the gas cools quite fast, yielding a temperature around 660 K for SEI = 0.7 eV molec^{-1} and 1756 K for SEI = 4.7 eV molec^{-1} already 50 µs after the pulse (cf. also Figure 1(f)). The electron temperature (T_e) is still more than ten times higher (i.e. T_e = 3.5 - 5 eV, or 40,600 K - 58,000 K), indicating that the plasma is clearly non-thermal for all conditions studied [5].

It is worth to mention that different pulse energies and different time between pulses, even if they result in the same overall SEI, can yield quite different values for the final gas temperature and gas temperature in the early afterglow , as can be seen when comparing Figure 5(c) for SEI = 1.7 eV molec^{-1} and Figure S.2(a) for SEI = 1.6 eV molec^{-1}. The final gas temperature and the gas temperature in the early afterglow are 1148 K and 3257 K, respectively, for SEI = 1.6 eV molec^{-1} and the corresponding values are 1029 K and 3911 K, respectively, for SEI = 1.7 eV molec^{-1}. In the latter case, higher pulse energies lead to higher gas temperatures just after the bursts, but the large time between bursts (3.33 ms) cools the mixture down more efficiently, resulting in a somewhat lower final gas temperature.

The calculated electron densities during the pulse vary from 5x10^{16} cm^{-3} to 8x10^{17} cm^{-3}, which corresponds well to experimental values obtained by Maqueo et al. [50] (i.e. ~1x10^{16} cm^{-3} for SEI < 0.6 eV molec^{-1} and around 3x10^{17} cm^{-3} for SEI = 0.7-2.0 eV molec^{-1} for CH_4 and CH_4/O_2 mixtures). Note that the electron densities are very high, due to the significant power density deposited during the ultrashort pulses, but these high densities are only reached for very short times. Both the electron temperature and density drop to negligible values in the afterglow of each pulse.

Finally, it is worth to stress that the CO_2 conversion is very high (reaching 100% at the highest SEI value; cf. Figure 7(d)) at the end of the pulse, but it drops dramatically in the

afterglow, as explained above, yielding a much lower overall CO_2 conversion when the gas mixture reaches the outlet at the grounded electrode (cf. Figure 4). Hence, the performance of NRP discharges could still be significantly improved if we could avoid this drop in CO_2 conversion upon pulse termination. Modelling can be very helpful to propose possible solutions for this, as we will illustrate in section 3.4 below.

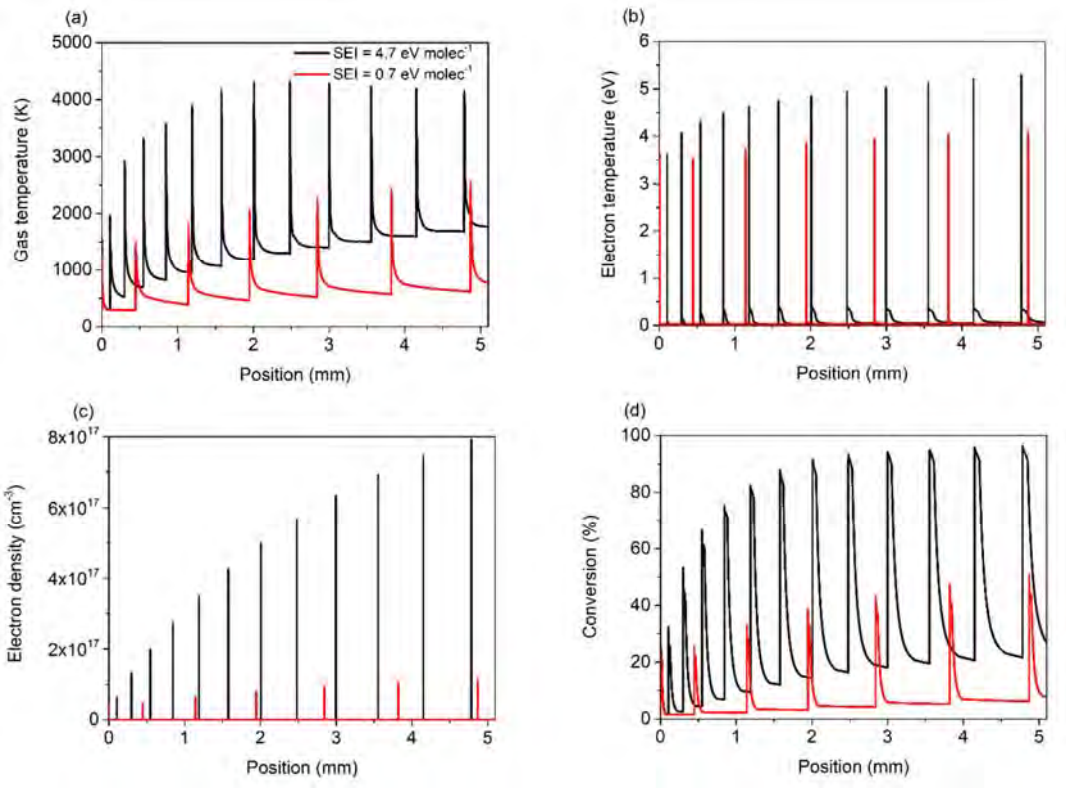

Figure 7: Calculated gas temperature (a), electron temperature (b), electron density (c), and CO_2 conversion (d), as a function of travelled distance between HV pin electrode and grounded electrode, for two different SEI values.

3.2 Chemical pathway analysis of CO_2 conversion

For all conditions studied, electron impact dissociation from vibrationally excited CO_2 is by far the dominant dissociation mechanism, with a relative contributions around 70 %, (see Figure 8). Electron impact dissociation from the CO_2 ground state contributes for about 10 %.

It should be stressed that electron dissociation is in fact electronic excitation towards a repulsive state, from which dissociation takes place. Therefore, although vibrational excitation is important, the reduced electric field reaches values above 200 Td inside the pulses, favoring electronic excitation-dissociation from the already vibrationally excited CO_2 levels. Dissociation from vibrationally excited CO_2 upon collision with an O atom or with any gas molecule M also occurs, but three-body recombination ($CO + O + M \rightarrow CO_2 + M$) is the dominant formation process of CO_2 (see SI: Figure S.3, panel (c)). As a result, the net contributions of dissociation upon collision with an O atom or any molecule M are at maximum only about 15 % and a few %, respectively (see Figure 8). The above recombination reaction, together with mixing of the converted gas with unreacted gas during expansion in the afterglow, seriously limits the efficiency of NRP-based CO_2 conversion, as explained above.

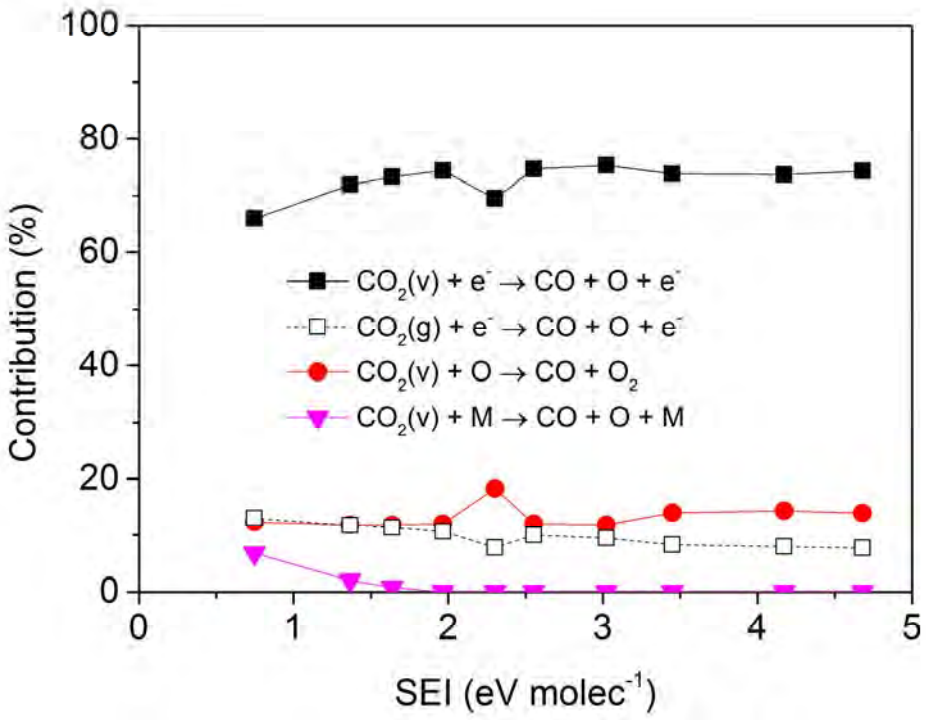

Figure 8: Relative net contributions of the main dissociation mechanisms of CO_2, as a function of SEI.

Our calculations reveal that the conversion mostly takes place during the pulses (~80 %) and a smaller fraction in the afterglows (~20 %) for all conditions studied (see Figure S.4 in the SI). However, during the afterglows, three-body recombination ($CO + O + M \rightarrow CO_2 + M$) compensates for the extra CO_2 conversion, and even goes faster than dissociation for the higher SEI values, so that a fraction of the converted CO_2 during the pulses is formed again in the afterglows (see Figure S.3 in the SI, panels (b) and (d)). Hence, it is clear that if this recombination reaction could be reduced, the performance of NRP discharges could be further enhanced.

3.3 Significant role of the CO_2 vibrational levels

From Figure 8 it is clear that vibrational excitation plays a crucial role for CO_2 dissociation at the conditions under study. Therefore, we plot the vibrational distribution function (VDF) in Figure 9, during the pulse (a) and at the end of the afterglow (b). During the pulse, there is obviously a high degree of vibrational excitation, with a large fraction of highly vibrationally excited CO_2, i.e., more than 20% is excited into the asymmetric mode levels V6 and higher. Their fraction even rises a bit towards the end of the pulse, as is clear from Figure 9(a). After the pulse, vibrational excitation stops, as the electrons do not gain energy anymore when there is no power deposition. At the same time, both VT relaxation (causing major heating immediately after pulse termination, as discussed above) and dissociation from these excited levels largely depopulate these levels. Therefore, when reaching the end of the afterglow, only the lowest vibrational levels are still significantly populated (Figure 9(b)). Note that the VDF at the end of the afterglow of the first pulse shows a considerably lower population of the higher levels than for the last pulse, and for the latter there is a large difference for different SEI values. This is simply due to the higher gas temperature (cf. Figure 7(a)), i.e., the VDFs more or less exhibit a thermal distribution, but there is no overpopulation anymore due to vibrational excitation.

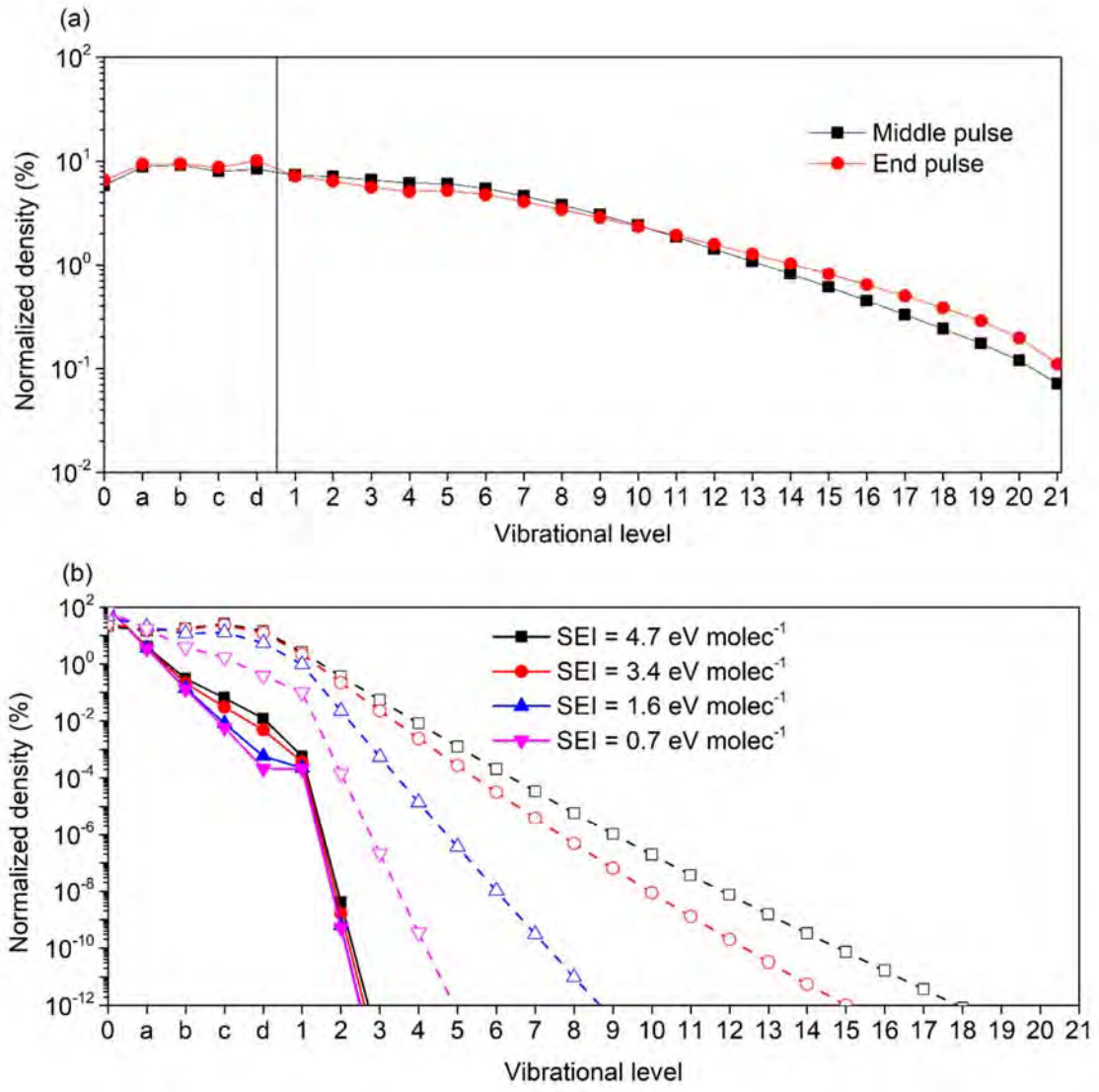

Figure 9: (a) Calculated VDF in the middle (5 ns) and at the end (10 ns) of the last pulse, at an SEI of 1.6 eV molec^{-1}. This result is representative for all pulses and all SEI values. (b) Calculated VDF at the end of the afterglow, for the first pulse (solid lines) and last pulse (dashed lines), for different SEI values. Note that "0" stands for the CO_2 ground state, "a-d" represent four effective symmetric mode levels at low energy, while "1-21" are the asymmetric mode vibrational levels up to the dissociation limit of 5.5 eV; see [32] for details.

Vibrational pumping during the pulses is thus important in NRP discharges, at least for the conditions investigated. As can be seen in Figure 10 for an SEI of 1.6 eV molec^{-1},

only 9 % of all CO_2 dissociation occurs from the ground state, while the rest is from the vibrational levels, albeit mainly (~ 67 %) from the lowest and middle levels (i.e., the four effective symmetric mode levels at low energy (Va-Vd) and the asymmetric mode levels V1-V15). Note that the lowest levels (i.e. the four effective symmetric mode levels at low energy (Va-Vd) and the first five asymmetric mode levels (V1-V5) have the highest contribution (~ 48 %), while the middle levels (i.e. V6-V15) only contribute for about 19 %, to the overall dissociation. In addition, 24 % of the total dissociation occurs from the highest asymmetric mode vibrational levels, which is quite striking and clearly indicates the overpopulation of these levels. Similar data are obtained at the other SEI values (Figure S.5 in the SI). Note that this figure only presents the contributions of the forward (dissociation) processes, not accounting for the reverse (recombination) reactions (see below).

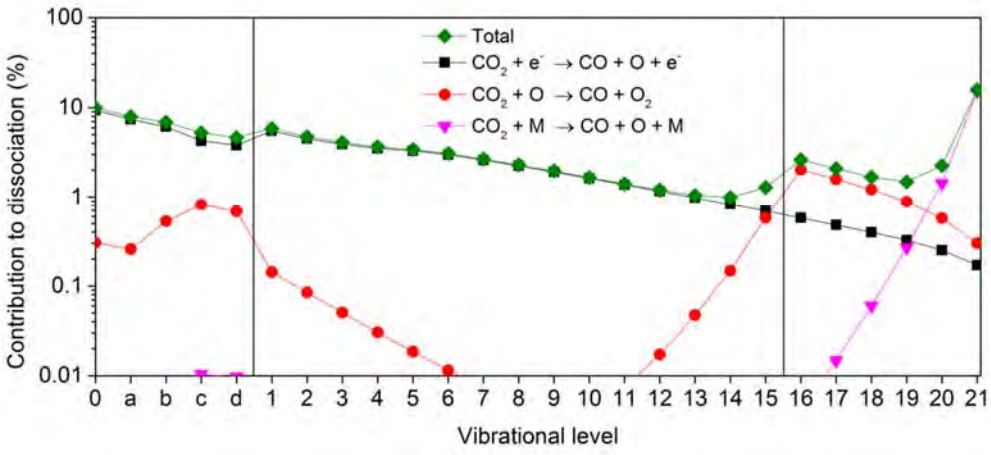

Figure 10: Contribution of the CO_2 ground state and the various vibrational levels to the total dissociation, as well as to the most important dissociation mechanisms, for an SEI of 1.6 eV molec^{-1}, only accounting for the forward reactions. The results for the other SEI values are illustrated in the SI.

When looking at the individual mechanisms (also plotted in Figure 10), electron impact dissociation through electronic excitation is by far the most important dissociation

mechanism for the lowest and middle levels (~94 %) (Va-Vd, and V1-V15), followed by dissociation upon collision with O atoms (~6 %). On the other hand, dissociation from the highest levels (V16-V21) is mainly due to dissociation upon collision with either an O atom (~49 %) or another molecule M (~28 %), while electron impact dissociation through electronic excitation contributes for ~23 %. Finally, dissociation from the ground state is mainly due to electron impact dissociation through electronic excitation (~97 %), but dissociation upon collision with an O atom also contributes for about 3 %. The latter process is possible since high gas temperatures can be reached, allowing thermal dissociation to occur. These relative contributions are also summarized in Table 3. Note that dissociation upon collision with another molecule M clearly becomes the dominant process for the highest vibrational levels, when only accounting for the forward reaction. However, when taking into account the reverse processes in the afterglow, i.e., three-body recombination ($CO + O + M \rightarrow CO_2 + M$), the net contribution of dissociation upon collision with another molecule M will become lower. We can thus conclude that overall, most dissociation occurs by electron impact from the lowest vibrational levels (i.e., Va-Vd, and V1-V5), i.e., about 48 %.

Table 3: Contribution of the CO_2 ground state, lowest and middle levels (Va-V15), and highest vibrational levels (V16-V21) to the total CO_2 dissociation (first row), and contribution of the different mechanisms to the dissociation of the ground state, lowest and middle levels, and highest vibrational levels of CO_2.

	Ground state	**Va-V15**	**V16-V21**
Total dissociation	9 %	67 %	24 %
$CO_2 + e^- \rightarrow CO + O + e^-$	97 %	94 %	23 %
$CO_2 + O \rightarrow CO + O_2$	3 %	6 %	49 %
$CO_2 + M \rightarrow CO + O + M$	0%	0 %	28 %

The vibrational kinetics thus play an important role in NRP discharges, explaining the promising conversions and energy efficiencies obtained (see Figure 4). When compared to reduced pressure MW plasmas, modelling predicts optimal conversions of around 20 %, with energy efficiencies of 30 %, in a pressure range of 200-300 mbar [7,51]. Van Rooij et al. [52] measured similar energy efficiencies (~30 %, but also up to ~45 %) with conversions of ~12 %, for pressures around 150-200 mbar, while at supersonic flows and reduced pressure, energy efficiencies around 90 % were experimentally found in 1983 [53], although these values have not been reproduced since then. Modelling showed that, at reduced pressure conditions, more than 70 % of all dissociation occurs through vibration-induced dissociation upon collision with O atoms or any other molecules M [7], and this is even more pronounced in supersonic flow conditions [54]. This process is in principle the most energy-efficient, and should be exploited. In our case, however, only about 15 % of the total dissociation is due to vibration-induced dissociation upon collision with O atoms (and only a few % due to collision with molecules M), as illustrated in Figure 8 above, which is attributed to the importance of the reverse (recombination) reaction ($CO + O + M \rightarrow CO_2 + M$), as explained above, thus limiting the conversion and energy efficiency. On the other hand, we still obtain maximum energy efficiencies of around 30 % at conversions around 15 %, for SEI = 1.4 eV molec^{-1}, and this is reached in subsonic flow conditions at atmospheric pressure, which is more suitable for industrial application and upscaling. Furthermore, NRP discharges seem to perform better than MW discharges at atmospheric pressure, where a maximum energy efficiency of 20 %, corresponding to a CO_2 conversion of around 10 % was obtained, at a flow rate of 16 slm and 1.5 kW plasma power [55]. In such MW plasma at atmospheric pressure, the vibrational levels are in thermal equilibrium, resulting in dissociation almost exclusively from the lowest levels and ground state [7], whereas in our case, more than 20 % of all dissociation occurs from the highest levels.

A gliding arc (GA) also operates at atmospheric pressure. In a classical GA, the conversion reaches up to 8 %, with energy efficiency up to 40% [11] In the Gliding Arc Plasmatron (GAP), a similar maximum conversions around 8 % is typically reached, with an energy efficiency around 30 % [14]. Hence, we obtain a somewhat higher conversion for the same energy efficiency in the NRP discharge. The reason is that both in a classical GA and GAP, CO_2 dissociation again almost exclusively occurs from the lowest vibrational levels, either by electron impact dissociation through electronic excitation or dissociation upon collision with O atoms or any molecules M [11], whereas in the NRP a significant portion of dissociation occurs from the highest levels (cf. Figure 10), which is more energy efficient.

Finally, when compared to DBD, where energy efficiencies and conversions are typically reported up to 10 % [4] (and clearly compete with each other, e.g., a maximum conversion of 30 % corresponds to an energy efficiency of only 2%, and a maximum energy efficiency of 8 % corresponds to a conversion of about 2 % [56]), the NRP discharge clearly performs better. Indeed, in DBDs, the energy efficient vibration-induced dissociation is found to be negligible [57].

3.4 Cooling as a solution to improve the CO_2 conversion and energy efficiency?

Although the NRP discharge exhibits already reasonable CO_2 conversion and energy efficiency, our simulations have also revealed the most important limitations, i.e., recombination in the afterglow (as well as mixing with fresh gas that has not passed through the plasma) and VT relaxation, causing thermalization of the VDF in the afterglow. Moreover, both processes cause significant heating, which induces even more recombination and VT relaxation (as the rate coefficients of both processes rise with temperature). Therefore, to stop this negative self-accelerating effect, we propose external cooling in the

afterglow, as a possible solution to improve the CO_2 conversion and energy efficiency in the NRP discharge.

Indeed, cooling can increase the non-equilibrium in the plasma, i.e., causing overpopulation of the vibrational levels, which may enhance the most energy efficient pathway of CO_2 conversion, i.e., through the vibrational levels. In fact, the most energy efficient process is through dissociation of the highest vibrational levels upon collision with either an O atom or another molecule M, as predicted by Berthelot and Bogaerts [7] . In addition, at lower temperature, the recombination reaction ($CO + O + M \rightarrow CO_2 + M$) in the afterglow might be reduced, thus also enhancing the net contribution of dissociation upon collision with molecules M (see above).

To verify the above hypotheses, we calculated the CO_2 conversion and corresponding energy efficiency for different cooling rates, and the results are plotted in Figure 11. These cooling rates are not fixed numbers, since we multiply the original cooling, which is dependent on the gas temperature and the plasma volume (c.f. equation 8 in the SI). However, we can calculate the average cooling rates throughout the whole simulation, which are 6.4×10^6 K s-1 for the original (turbulent) cooling, 8.6×10^6 K s^{-1} for cooling x 2, 1.2×10^7 K s^{-1} for cooling x 5 and 1.4×10^7 K s^{-1} for cooling x 10. These extra cooling rates are in first instance an academic exercise. However, there are some practical possibilities to provide extra cooling. One way could be to reduce the external pressure, resulting in a higher expansion velocity, causing a larger cooling effect. Another way is to use a chemical inert gas as an extra cooling agent. Still another possibility could be water cooling, in which the CO_2 flux enters a water-cooled tube with a radius much smaller than the 35 mm diameter of the actual chamber, in which gas expansion is still possible, causing recirculation of the gas, which has been extra cooled by the wall. Finally, pre-cooling the mixture will result in a more

efficient cooling in the afterglow because of mixing with a cold gas. Nevertheless, these possibilities still need to be evaluated in practice. In this paper we illustrate how cooling, in any form, can affect the vibrational kinetics and dissociation mechanisms, without worrying about the practical implementations for now. The original cooling was depicted in Figure 5(a) for SEI = 1.7 eV molec^{-1}, and is similar for the other SEI values as well (cf. Figure 7 and Figure S.2 in SI). A cooling rate twice as high has very little effect, but a five times higher cooling rate can enhance the conversion and energy efficiency up to a factor 1.7, at least for SEI values below 2.3 eV molec^{-1}. Likewise, ten times higher cooling yields an improvement in conversion and energy efficiency up to a factor 2.2.

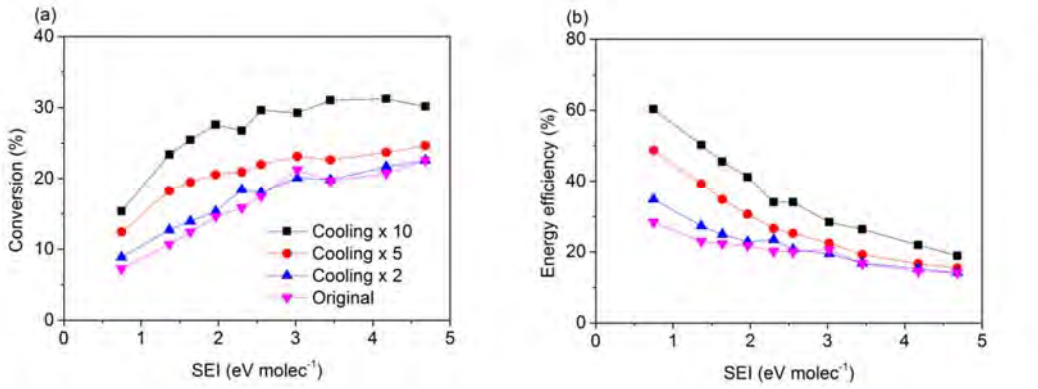

Figure 11: Calculated conversions (a) and energy efficiencies (b) as a function of SEI, for different cooling rates.

The resulting gas temperatures as a function of travelled distance from HV electrode to grounded electrode, i.e., passing several pulses and afterglows, are depicted in Figure S.6 in SI, for these different cooling rates, and for the lowest, highest and an intermediate SEI value. Table 4 summarizes the maximum gas temperature and the temperature at the end of the afterglow, for the last pulse, calculated by the original model and when applying the different cooling rates, for three different SEI values, i.e. 0.7 eV molec^{-1}, 1.6 eV molec^{-1} and 4.7 eV molec^{-1}. The maximum gas temperature reduces by only a factor 1.3 when applying a

cooling rate twice as high as the original cooling, while it reduces by a factor 1.7 and 2.2 when applying a five or ten times higher cooling rate. This will affect the chemistry, as most rate coefficients are a function of temperature.

Table 4: Effect of the cooling rate on the maximum gas temperature and the gas temperature at the end of the afterglow for different SEI values.

Temperature (K)	**At maximum**			**At end of afterglow**		
At SEI (eV molec^{-1})	0.7	1.6	4.7	0.7	1.6	4.7
Original	2553	3257	4155	660	1148	1756
Cooling x2	2007	2623	3774	488	909	1450
Cooling x5	1531	1892	3091	348	628	1102
Cooling x10	1306	1417	2431	305	448	822

Figure 12 illustrates the relative net contributions of the different dissociation processes, as a function of SEI, for twice (a), five times (b) and ten times (c) higher cooling rate. While electron impact dissociation through electronic excitation from the CO_2 vibrational levels is still the dominant dissociation process, dissociation upon collision with another molecule M gradually becomes more important, at least for the lower SEI values. Indeed, while its contribution was only 1 % in the original model at an SEI value of 1.6 eV molec^{-1} (cf. Figure 8), it is 3 %, 8 % and 23 % when applying twice, five times and ten times faster cooling, respectively. The reason is indeed as hypothesized above, i.e., the recombination reaction ($CO + O + M \rightarrow CO_2 + M$) drops at lower temperature, thus increasing the net contribution of the dissociation pathway upon collision with molecules M,

especially from the highest vibrational levels. Indeed, Figure S.7 in SI shows the net contribution of the different vibrational levels to the total CO_2 dissociation, for the original model and with cooling rates times two, five and ten. It can be deduced that the net contribution of the highest vibrational levels (V16-V21) towards CO_2 dissociation increases from 14 % in the original model, to 23 %, 35% and 39 % on average, at a cooling rate times two, five, and ten, respectively, at SEI values below 2.3 eV molec^{-1}. Only at the two lowest SEI values studied, i.e., SEI = 0.7 eV molec^{-1} and 1.4 eV molec^{-1}, a ten times higher cooling rate does not promote extra dissociation upon collision with another molecule M. Indeed, the electron density also drops about a factor two at a cooling rate times ten compared to original cooling. This causes less vibrational excitation, and thus a lower population of the highest vibrational levels, and therefore less dissociation from these levels. However, cooling also reduces gas expansion and results in a longer residence time and higher conversion and energy efficiency.

In general, as dissociation upon collision with molecules M, especially from the higher vibrational levels, is the most energy efficient CO_2 dissociation mechanism (see above), the increasing contribution of this process explains the higher and more energy efficient CO_2 conversion at higher cooling rates, as predicted by the model (cf. Figure 11).

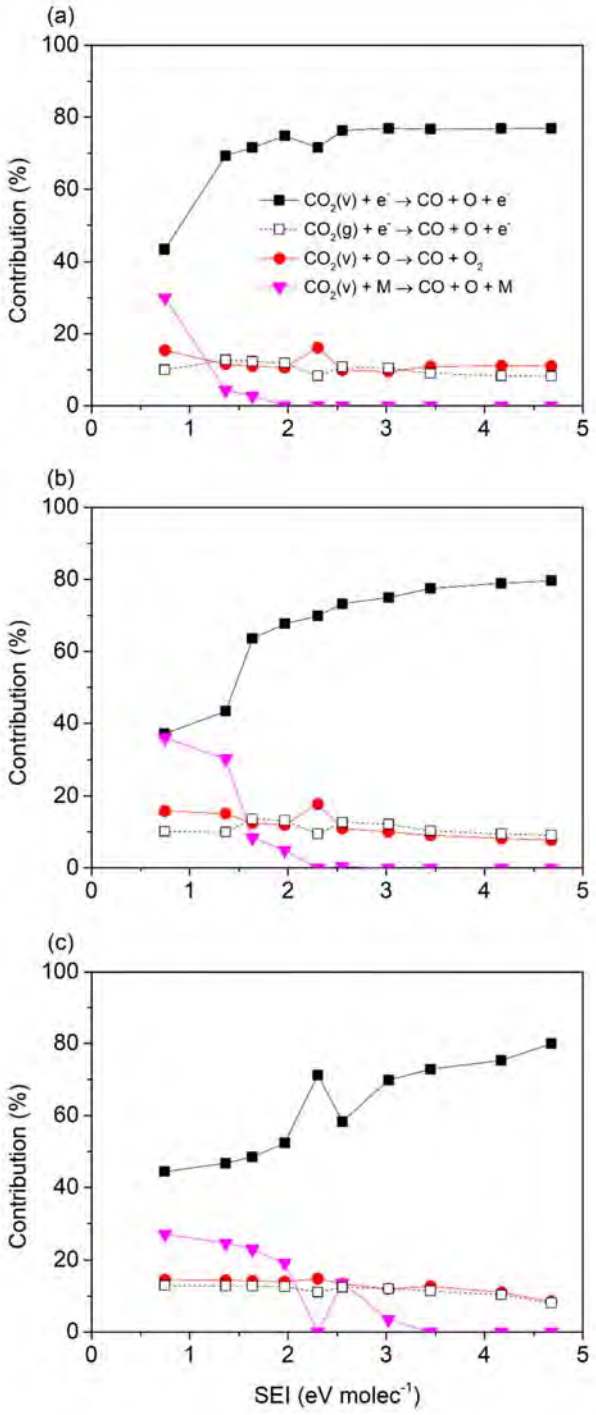

Figure 12: Net contribution of the different dissociation processes as a function of SEI, for a cooling rate twice (a), five times (b) and ten times (c) higher than in the original model. The results should be compared with Figure 8 above.

One could expect that the VDF would also show more pronounced overpopulation of the higher vibrational levels at higher cooling rates, but this is not predicted by the model (cf. Figure S.8 in the SI). Indeed, the VDF at the end of the pulse is almost not affected, while the VDF at the end of the afterglow drops faster for the higher levels upon higher cooling. The latter can be explained by the fact that the VDFs are anyway thermalized at the end of the afterglow, and a lower gas temperature (upon higher cooling) thus causes a faster drop of the VDF. The fact that the VDF during the pulse is not affected, might at first sight be unexpected, as the lower VT rates would cause a more pronounced overpopulation of the higher vibration levels. However, the latter is compensated by the loss of these higher vibrational levels due to dissociation upon collision with other molecules M, as illustrated in Figures 12 and S.7. Thus, although the net effect on the VDF is negligible, the loss process of these high vibrational levels is different: they do not get lost in VT relaxation (which is a pure loss process), but they are used for the most energy efficient CO_2 dissociation process, explaining the rise in CO_2 conversion and energy efficiency, as illustrated in Figure 11 above.

It should be noted that applying extra cooling will also cost energy, so it will increase the SEI in practice, which is not accounted for in our simulations. Therefore, the enhancement in energy efficiency will be less pronounced as predicted by our model. However, conceptual studies like these are interesting to pinpoint how in theory it is possible to reach more energy efficient CO_2 conversion in NRP discharges. In summary, our model predicts that a higher cooling reduces both VT relaxation and the recombination reaction ($CO + O + M \rightarrow CO_2 + M$) in the afterglow, so that the net contribution of dissociation of the higher vibrational levels upon collision with molecules M rises, and this generally explains the higher CO_2 conversion and energy efficiency.

4. Conclusion

We developed a chemical kinetics model to elucidate the main dissociation mechanisms of CO_2 in an NRP discharge. We compared the calculated conversions and energy efficiencies with experimental results in a wide range of SEI values, as well as the evolution of gas temperature and CO_2 conversion in the afterglow. The calculation results are in satisfactory agreement with the experiments, which indicates that our model can provide a realistic picture of the underlying chemistry in the NRP discharge, and can be used to identify its limitations and suggest further improvements.

The NRP discharge shows promising results for both CO_2 conversion and energy efficiency (or energy cost), by stimulating vibrational excitation. Indeed, more than 20 % of all CO_2 dissociation occurs from the highest asymmetric stretch mode levels (V16-V21), mainly by dissociation upon collision with an O atom or with another molecule M, while 67 % of the dissociation occurs from the lowest and middle levels (Va-Vd, and V1-V15) and 9 % from the CO_2 ground state, mainly by electron impact dissociation through electronic excitation. However, in between the pulses (i.e., during the so-called afterglows), fresh gas entering the plasma, VT relaxation (depopulating the higher vibrational levels) and recombination reactions (mainly $CO + O + M \rightarrow CO_2 + M$), limit the conversion and energy efficiency. The latter two processes also induce intense heating just after the pulses, causing self-acceleration, as both processes are enhanced at higher gas temperature. Nevertheless, the performance of the NRP discharge is very competitive with other plasma sources used for CO_2 conversion.

To further improve the performance, we propose extra cooling in the afterglows. Our model predicts that a five or ten times higher cooling rate can increase both the conversion and energy efficiency by about a factor 2, for SEI values below 2.3 eV molec^{-1}. Indeed, in general, extra cooling slows down the rate of the recombination reaction ($CO + O + M \rightarrow$

CO_2 + M) and enhances the contribution of the highest vibrational levels in the overall CO_2 dissociation, making the conversion more energy efficient. However, we must note that the energy cost for extra cooling was not yet taken into account, so the improvement in energy efficiency will be somewhat overestimated. Nevertheless, this conceptual study is very useful to reveal how more energy efficient CO_2 conversion can be reached in NRP discharges. We hope that these predictions can inspire other groups to evaluate the effect of cooling in practice.

5. Description of Supporting Information

The Supporting Information contains a more detailed description of the 0D model. We also plot the energy deposited per pulse, the frequency and the corresponding number of pulses, as a function of SEI, as well as the calculated gas temperature, electron temperature, electron density and CO_2 conversion as a function of travelled distance between pin HV electrode and grounded electrode, for two different SEI values (different from those shown in the paper, i.e., 1.6 eV molec^{-1} and 3.4 eV molec^{-1}). Furthermore, we show more details on the CO_2 dissociation and formation mechanisms, both overall and specifically in the afterglow, as well as the contribution of the different vibrational levels to the overall CO_2 dissociation, for other SEI values than shown in the paper (i.e., 0.7 eV molec^{-1}, 3.4 eV molec^{-1} and 4.7 eV molec^{-1}). Finally, the effect of cooling on the evolution of the gas temperature as a function of travelled distance between pin HV electrode and grounded electrode for different SEI values (i.e., 0.7 eV molec^{-1}, 1.6 eV molec^{-1} and 4.7 eV molec^{-1}), on the net contribution of the different vibrational levels to the overall CO_2 dissociation for different SEI values, and on the VDF (at SEI = 1.6 eV molec^{-1}) at the end of the pulse and afterglow is shown.

6. Acknowledgements

The authors acknowledge financial support from the Fund for Scientific Research – Flanders (FWO; Grant no. G.0383.16N).

7. Bibliography

(1) Blunden, J.; Arndt, D. S. State of the Climate in 2015. *Bull. Amer. Meteor. Soc.* **2016**, *97*, S1–S275.

(2) UNFCCC. *Report of the Conference of the Parties on Its Twenty-First Session, Held in Paris from 30 November to 13 December 2015*; 2015.

(3) McDonough, W.; Braungart, M.; Anastas, P. T.; Zimmerman, J. B. Peer Reviewed: Applying the Principles of Green Engineering to Cradle-to-Cradle Design. *Environ. Sci. Technol.* **2003**, *37*, 434A–441A.

(4) Snoeckx, R.; Bogaerts, A. Plasma Technology-a Novel Solution for CO_2 Conversion? *Chem. Soc. Rev.* **2017**, *46*, 5805–5863.

(5) Fridman, A. *Plasma Chemistry*; Cambridge University Press: New York, U.S.A., 2008.

(6) Bongers, W.; Bouwmeester, H.; Wolf, B.; Peeters, F.; Welzel, S.; van den Bekerom, D.; den Harder, N.; Goede, A.; Graswinckel, M.; Groen, P. W.; et al. Plasma-Driven Dissociation of CO2 for Fuel Synthesis. *Plasma Process. Polym.* **2017**, *14*, e1600126.

(7) Berthelot, A.; Bogaerts, A. Modeling of CO_2 Splitting in a Microwave Plasma: How to Improve the Conversion and Energy Efficiency. *J. Phys. Chem. C* **2017**, *121*, 8236–8251.

(8) Spencer, L. F.; Gallimore, A. D. Efficiency of CO_2 Dissociation in a Radio-Frequency Discharge. *Plasma Chem. Plasma Process.* **2011**, *31*, 79–89.

(9) Trenchev, G.; Nikiforov, A.; Wang, W.; Kolev, S.; Bogaerts, A. Atmospheric Pressure Glow

Discharge for CO2 Conversion : Model-Based Exploration of the Optimum Reactor Configuration. *Chem. Eng. J.* **2019**, *362*, 830–841.

(10) Indarto, A.; Choi, J.; Lee, H.; Song, H. K. Conversion of CO_2 by Gliding Arc Plasma. *Environ. Eng. Sci.* **2012**, *23*, 1033–1043.

(11) Sun, S. R.; Wang, H. X.; Mei, D. H.; Tu, X.; Bogaerts, A. CO_2 Conversion in a Gliding Arc Plasma: Performance Improvement Based on Chemical Reaction Modeling. *J. CO2 Util.* **2016**, *17*, 220–234.

(12) Nunnally, T.; Gutsol, K.; Rabinovich, A.; Fridman, A.; Gutsol, A.; Kemoun, A. Dissociation of CO_2 in a Low Current Gliding Arc Plasmatron. *J. Phys. D. Appl. Phys.* **2011**, *44*, 274009.

(13) Nunnally, T. P. Application of Low Current Gliding Arc Plasma Discharges for Hydrogen Sulfide Decomposition and Carbon Dioxide Emission Reduction, PhD Dissertation, Drexel University, PhD Thesis, Drexel University, 2011.

(14) Ramakers, M.; Trenchev, G.; Heijkers, S.; Wang, W.; Bogaerts, A. Gliding Arc Plasmatron: Providing a Novel Method for Carbon Dioxide Conversion. *Chem. Sus. Chem.* **2017**, *10*, 2642–2652.

(15) Trenchev, G.; Kolev, S.; Wang, W.; Ramakers, M.; Bogaerts, A. CO_2 Conversion in a Gliding Arc Plasmatron: Multidimensional Modeling for Improved Efficiency. *J. Phys. Chem. C* **2017**, *121*, 24470–24479.

(16) Liu, J. L.; Park, H. W.; Chung, W. J.; Park, D. W. High-Efficient Conversion of CO_2 in AC-Pulsed Tornado Gliding Arc Plasma. *Plasma Chem. Plasma Process.* **2016**, *36*, 437–449.

(17) Zhang, J. Q.; Yang, Y. J.; Zhang, J. S.; Liu, Q. Study on the Conversion of CH_4 and CO_2 Using a Pulsed Microwave Plasma under Atmospheric Pressure. *Acta Chim. Sin.* **2002**, *60*, 1973–1980.

(18) Cleiren, E.; Heijkers, S.; Ramakers, M.; Bogaerts, A. Dry Reforming of Methane in a Gliding Arc Plasmatron: Towards a Better Understanding of the Plasma Chemistry. *Chem. Sus. Chem.* **2017**, *10*, 4025–4036.

(19) Tu, X.; Gallon, H. J.; Twigg, M. V; Gorry, P. A.; Whitehead, J. C. Dry Reforming of Methane over a Ni / Al_2O_3 Catalyst in a Coaxial Dielectric Barrier Discharge Reactor. *J. Phys. D Appl. Phys.* **2011**, *44*, 274007.

(20) Wang, Q.; Yan, B. H.; Jin, Y.; Cheng, Y. Dry Reforming of Methane in a Dielectric Barrier Discharge Reactor with Ni/Al_2O_3 Catalyst: Interaction of Catalyst and Plasma. *Plasma Chem. Plasma Process.* **2009**, *29*, 217–228.

(21) Snoeckx, R.; Aerts, R.; Tu, X.; Bogaerts, A. Plasma-Based Dry Reforming: A Computational Study Ranging from the Nanoseconds to Seconds Time Scale. *J. Phys. Chem. C* **2013**, *117*, 4957–4970.

(22) Gallon, H. J.; Tu, X.; Whitehead, J. C. Effects of Reactor Packing Materials on H_2 Production by CO_2 Reforming of CH_4 in a Dielectric Barrier Discharge. *Plasma Process. Polym.* **2012**, *9*, 90–97.

(23) Scapinello, M.; Martini, L. M.; Tosi, P. CO_2 Hydrogenation by CH_4 in a Dielectric Barrier Discharge: Catalytic Effects of Nickel and Copper. *Plasma Process. Polym.* **2014**, *11*, 624–628.

(24) Martini, L. M.; Dilecce, G.; Guella, G.; Maranzana, A.; Tonachini, G.; Tosi, P. Oxidation of CH_4 by CO_2 in a Dielectric Barrier Discharge. *Chem. Phys. Lett.* **2014**, *593*, 55–60.

(25) Snoeckx, R.; Ozkan, A.; Reniers, F.; Bogaerts, A. The Quest for Value-Added Products from Carbon Dioxide and Water in a Dielectric Barrier Discharge: A Chemical Kinetics Study. *ChemSusChem* **2017**, *10*, 409–424.

(26) Snoeckx, R.; Heijkers, S.; Van Wesenbeeck, K.; Lenaerts, S.; Bogaerts, A. CO_2 Conversion in a

Dielectric Barrier Discharge Plasma: N_2 in the Mix as a Helping Hand or Problematic Impurity? *Energy Environ. Sci.* **2016**, *9*, 30–39.

(27) Heijkers, S.; Snoeckx, R.; Kozak, T.; Silva, T.; Godfroid, T.; Britun, N.; Snyders, R.; Bogaerts, A. CO_2 Conversion in a Microwave Plasma Reactor in the Presence of N_2 : Elucidating the Role of Vibrational Levels. *J. Phys. Chem. C* **2015**, *119*, 12815–12828.

(28) Kano, M.; Satoh, G.; Iizuka, S. Reforming of Carbon Dioxide to Methane and Methanol by Electric Impulse Low-Pressure Discharge with Hydrogen. *Plasma Chem. Plasma Process.* **2012**, *32*, 177–185.

(29) Scapinello, M.; Martini, L. M.; Dilecce, G.; Tosi, P. Conversion of CH4 /CO2 by a Nanosecond Repetitively Pulsed Discharge. *J. Phys. D. Appl. Phys.* **2016**, *49*, 075602–075609.

(30) Martini, L. M.; Lovascio, S.; Dilecce, G.; Tosi, P. Time-Resolved CO_2 Dissociation in a Nanosecond Pulsed Discharge. *Plasma Chem. Plasma Process.* **2018**, *38*, 707–718.

(31) Martini, L. M.; Gatti, N.; Dilecce, G.; Scotoni, M.; Tosi, P. Laser Induced Fluorescence in Nanosecond Repetitively Pulsed Discharges for CO_2 Conversion. *Plasma Phys. Control. Fusion* **2018**, *60*, 014016.

(32) Kozák, T.; Bogaerts, A. Splitting of CO_2 by Vibrational Excitation in Non-Equilibrium Plasmas: A Reaction Kinetics Model. *Plasma Sources Sci. Technol.* **2014**, *23*, 045004.

(33) Berthelot, A.; Bogaerts, A. Modeling of CO_2 Plasma: Effect of Uncertainties in the Plasma Chemistry. *Plasma Sources Sci. Technol.* **2017**, *26*, 115002.

(34) Phelps, A. V. Phelps Database www.lxcat.net.

(35) Lowke, J. J.; Phelps, A. V.; Irwin, B. W. Predicted Electron Transport Coefficients and Operating Characteristics of CO_2/N_2/He Laser Mixtures. *J. Appl. Phys.* **1973**, *44*, 4664–4671.

(36) Hake, R. D.; Phelps, A. V. Momentum-Transfer and Inelastic-Collision Cross Sections for Electrons in O_2, CO, and CO_2. *Phys. Rev.* **1967**, *158*, 70–84.

(37) Grofulovic, M.; Alves, L. L.; Guerra, V. Electron-Neutral Scattering Cross Sections for CO_2 a Complete and Consistent Set and an Assessment of Dissociation. *J. Phys. D Appl. Phys.* **2016**, *49*, 395207.

(38) Bogaerts, A.; Wang, W.; Berthelot, A.; Guerra, V. Modeling Plasma-Based CO_2 Conversion : Crucial Role of the Dissociation Cross Section. *Plasma Sources Sci. Technol.* **2016**, *25*, 055016.

(39) Pietanza, L. D.; Colonna, G.; D'Ammando, G.; Laricchiuta, A.; Capitelli, M. Vibrational Excitation and Dissociation Mechanisms of CO_2 under Non-Equilibrium Discharge and Post-Discharge Conditions. *Plasma Sources Sci. Technol.* **2015**, *24*, 042002.

(40) Pietanza, L. D.; Colonna, G.; D'Ammando, G.; Laricchiuta, A.; Capitelli, M. Electron Energy Distribution Functions and Fractional Power Transfer in "Cold" and Excited CO_2 Discharge and Post Discharge Conditions. *Phys. Plasmas* **2016**, *23*, 013515.

(41) Pietanza, L. D.; Colonna, G.; D'Ammando, G.; Laricchiuta, A.; Capitelli, M. Non Equilibrium Vibrational Assisted Dissociation and Ionization Mechanisms in Cold CO_2 Plasmas. *Chem. Phys.* **2016**, *468*, 44–52.

(42) Stancu, G. D.; Kaddouri, F.; Lacoste, D. A.; Laux, C. O. Atmospheric Pressure Plasma Diagnostics by OES, CRDS and TALIF. *J. Phys. D. Appl. Phys.* **2010**, *43*, 124002.

(43) Castela, M.; Stepanyan, S.; Fiorina, B.; Coussement, A.; Gicquel, O.; Darabiha, N.; Laux, C. O. A 3-D DNS and Experimental Study of the Effect of the Recirculating Flow Pattern inside a Reactive Kernel Produced by Nanosecond Plasma Discharges in a Methane-Air Mixture. *Proc. Combust. Inst.* **2017**, *36*, 4095–4103.

(44) Lo, A.; Cessou, A.; Boubert, P.; Vervisch, P. Space and Time Analysis of the Nanosecond Scale

Discharges in Atmospheric Pressure Air: I. Gas Temperature and Vibrational Distribution Function of N2 and O2. *J. Phys. D. Appl. Phys.* **2014**, *47*, 115201.

(45) Popov, N. A. Pulsed Nanosecond Discharge in Air at High Specific Deposited Energy: Fast Gas Heating and Active Particle Production. *Plasma Sources Sci. Technol.* **2016**, *25*, 044003.

(46) Kozak, T.; Bogaerts, A. Evaluation of the Energy Efficiency of CO_2 Conversion in Microwave Discharges Using a Reaction Kinetics Model. *Plasma Sources Sci. Technol.* **2015**, *24*, 015024.

(47) Da, X. Thermal and Hydrodynamic Effects of Nanosecond Discharges in Air and Application to Plasma-Assisted Combustion, CNRS, 2013.

(48) Pinhão, N. R.; Moura, A.; Branco, J. B.; Neves, J. Influence of Gas Expansion on Process Parameters in Non-Thermal Plasma Plug-Flow Reactors: A Study Applied to Dry Reforming of Methane. *Int. J. Hydrogen Energy* **2016**, *41*, 9245–9255.

(49) Seydou, A.; Claverie, A.; Sotton, J.; Bellenoue, M. Experimental Investigation of the Effects of Nanosecond Repetitive Pulsed (NRP) Discharges on Ignition of Methane-Air Mixtures. In *18th International Symposium on the Application of Laser and Imaging Techniques to Fluid Mechanics Lisbon(Portugal)*; 2016.

(50) Maqueo, P. D. G.; Maier, M.; Evans, M. D. G.; Coulombe, S.; Bergthorson, J. M. Regimes of an Atmospheric Pressure Nanosecond Repetitively Pulsed Discharge for Methane Partial Oxidation. *J. Phys. D. Appl. Phys.* **2018**, *51*, 134005.

(51) Bogaerts, A.; Berthelot, A.; Heijkers, S.; Kolev, S.; Snoeckx, R.; Sun, S.; Trenchev, G.; Van Laer, K.; Wang, W. CO_2 Conversion by Plasma Technology: Insights from Modeling the Plasma Chemistry and Plasma Reactor Design. *Plasma Sources Sci. Technol.* **2017**, *26* (6).

(52) van Rooij, G. J.; van den Bekerom, D. C. M.; den Harder, N.; Minea, T.; Berden, G.; Bongers, W. A.; Engeln, R.; Graswinckel, M. F.; Zoethout, E.; van de Sanden, M. C. M. Taming

Microwave Plasma to Beat Thermodynamics in CO_2 Dissociation. *Faraday Discuss.* **2015**, *183*, 233–248.

(53) Asisov, R. I.; Givotov, V. K.; Krasheninnikov, E. G.; Potapkin, B. V.; Rusanov, V. D.; Fridman, A. Carbon Dioxide Dissociation in Non-Equilibrium Plasma. *Sov. Phys. Dokl.* **1983**, *271*, 94.

(54) Vermeiren, V.; Bogaerts, A. Supersonic Microwave Plasma: Potential and Limitations for Energy-Efficient CO2 Conversion. *J. Phys. Chem. C* **2018**, *122*, 25869–25881.

(55) Spencer, L. F.; Gallimore, a D. CO_2 Dissociation in an Atmospheric Pressure Plasma/Catalyst System: A Study of Efficiency. *Plasma Sources Sci. Technol.* **2013**, *22*, 015019.

(56) Aerts, R.; Somers, W.; Bogaerts, A. Carbon Dioxide Splitting in a Dielectric Barrier Discharge Plasma: A Combined Experimental and Computational Study. *ChemSusChem* **2015**, *8*, 702–716.

(57) Aerts, R.; Martens, T.; Bogaerts, A. Influence of Vibrational States on CO2 Splitting by Dielectric Barrier Discharges. *J. Phys. Chem. C* **2012**, *116*, 23257–23273.

8.0 TOC

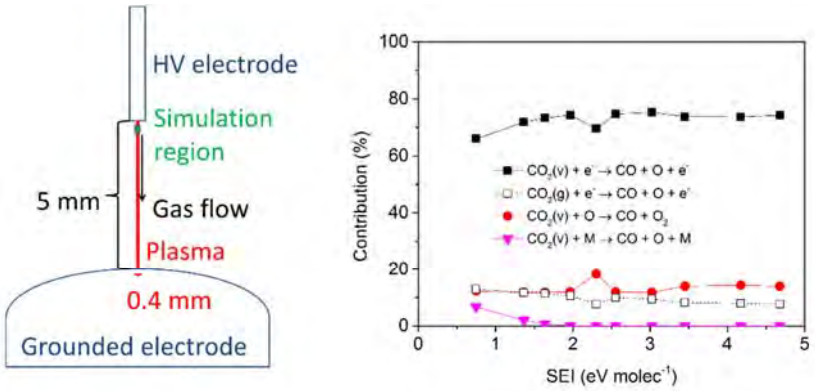
HV electrode
Simulation region
5 mm
Gas flow
Plasma
0.4 mm
Grounded electrode
Contribution (%)
SEI (eV molec-1)
CO2(v) + e- → CO + O + e-
CO2(g) + e- → CO + O + e-
CO2(v) + O → CO + O2
CO2(v) + M → CO + O + M

Supporting Information: Nanosecond Pulsed Discharge for CO_2 Conversion: Kinetic Modelling to Elucidate the Chemistry and Improve the Performance

Stijn Heijkers[1] , Luca Matteo Martini[2,†], Giorgio Dilecce[3,2], Paolo Tosi[2,3] and Annemie Bogaerts[1]*

[1] Research group PLASMANT, Department of Chemistry, University of Antwerp, Universiteitsplein 1, BE-2610 Wilrijk-Antwerp, Belgium

*annemie.bogaerts@uantwerpen.be, +3232652377

[2] Dipartimento di Fisica, Università di Trento, Italy

[3] P.Las.Mi Lab NANOTEC – CNR Bari, Italy

[†] Present address: Department of Applied Physics, Eindhoven University of Technology, The Netherlands

Contents

1. Detailed description of the model

The 0D model is based on solving equation (1):

$$\frac{\partial n_s}{\partial t} = \sum_{i=1}^{j}\left[\left(a_{s,i}^{R} - a_{s,i}^{L}\right)R_i\right] \quad (1)$$

where n_s is the density of species s (in m^{-3}) , j the total number of reactions, $a_{s,i}^L$ and $a_{s,i}^R$ the stoichiometric coefficients at the left hand side and right hand side of the reaction and R_i the rate of reaction (in m^{-3} s^{-1}), given by:

$$R_i = k_i \prod_s n_s^{a_{s,i}} \quad (2)$$

where k_i is the rate constant (in m^3 s^{-1} or m^6 s^{-1} for two-body or three-body reactions, respectively) and $a_{s,i}$ was defined above. The rate constants of the heavy particle reactions are either constant or dependent on the gas temperature, whereas the rate constants of the electron impact reactions depend on the electron temperature T_e or the reduced electric field E/N (i.e., the electric field E divided by the number density of all neutral species N, usually expressed in Td = 10^{-21} V m^2). The rate constants of the electron impact reactions are generally calculated according to the following equation:

$$k_i = \int_{\varepsilon_{th}}^{\infty} \sigma_i(\varepsilon) v(\varepsilon) f(\varepsilon) d\varepsilon \quad (3)$$

with ε the electron energy (usually in eV), ε_{th} the minimum threshold energy needed to induce the reaction, $v(\varepsilon)$ the velocity of the electrons (in m s^{-1}) , $\sigma_i(\varepsilon)$ the cross section of collision i (in m^2), and $f(\varepsilon)$ the (normalized) electron energy distribution function (EEDF; in eV^{-1}) calculated using a Boltzmann solver. The reactions included in the model, along with their rate coefficients and the references where these data are adopted from, are listed in Tables S.1-S.5.

In this work we use the ZDPlaskin code [1] to solve the balance equations (1) of all species, which also has a built-in Boltzmann solver, called BOLSIG+ [2], to calculate the EEDF and the rate constants of the electron impact reactions based on a set of cross sections, the plasma composition, the gas temperature and the reduced electric field (E/N).

The electric field (E; in V m^{-1}) is calculated from a given power density, using the so-called local field approximation [3]:

$$E = \sqrt{\frac{P}{\sigma}} \quad (4)$$

with P the input power density (in W m^{-3}) and σ the plasma conductivity (A V^{-1} m^{-1}). The plasma conductivity is estimated at the beginning of the simulations as [3]:

$$\sigma = \frac{e^2 n_{e,init}}{m_e \nu_m} \quad (5)$$

with e the elementary charge (1.6022x10^{-19} C), $n_{e,init}$ the initial electron density (in m^{-3}), m_e the electron mass (9.1094x10^{-31} kg) and ν_m the collision frequency (in s^{-1}) calculated using BOLSIG+. During the simulation the plasma conductivity is calculated as [3]:

$$\sigma = \frac{e v_d n_e}{(\frac{E}{N})_{prev} n_0} \quad (6)$$

with v_d the electron drift velocity (in m s^{-1}), which is calculated using BOLSIG+ implemented in ZDPlaskin, and $(\frac{E}{N})_{prev}$ the reduced electric field at the previous time step (in V m^2).

The balance equation for the gas temperature T_g (in K) is also solved:

$$N \frac{\gamma k}{\gamma - 1} \frac{dT_g}{dt} = P_{e,el} + \sum_j R_j \Delta H_j - P_{ext} \quad (7)$$

where $N = \sum n_i$ is the total neutral species density, γ is the specific heat ratio of the total gas mixture, k is the Boltzmann constant (in J K^{-1}), $P_{e,el}$ is the gas heating power density due to elastic electron-neutral collisions (in W m^{-3}), R_j is the rate of reaction j (in m^{-3} s^{-1}), ΔH_j is the heat released (or consumed when this value is negative) by reaction j (in J) and P_{ext} is the heat loss due to energy exchange with the surroundings (in W m^{-3}). The latter one is originally calculated as:

$$P_{ext} = \frac{8\lambda}{R^2}(T_g - T_{g,i}) \quad (8)$$

where λ is the gas thermal conductivity (in W m^{-1} K^{-1}), R the radius of the plasma zone, T_g the plasma gas temperature and $T_{g,i}$ the gas temperature just before the start of the pulse, i.e. 293.15 K at the beginning of the simulation, or the gas temperature at the end of the afterglow of the previous pulse (see main text for more explanation).

Greig et al.[4] and Shneider [5] showed that in ns-pulsed discharges turbulent cooling is important. Therefore, we multiply equation (8) by a factor 9 to incorporate the more effective turbulent cooling, which is also successfully applied in 0D simulations for a turbulent GAP [6–8], with this factor based on 2D fluid dynamics simulations [9].

The specific heat ratio of the total (ideal) gas mixture is calculated from the specific heat ratios of the individual species in the model, γ_i, using the formula:

$$N\frac{\gamma}{\gamma-1} = \sum_i n_i \frac{\gamma_i}{\gamma_i-1} \quad (9)$$

where n_i are the densities of the individual species i. The individual specific heat ratios, γ_i, can be calculated from the specific heat capacity at constant pressure $c_{p,i}$ (in J K^{-1} kg^{-1}) using the relation:

$$c_{p,i} = \frac{\gamma_i}{\gamma_i-1}\frac{k}{M} \quad (10)$$

where k is the Boltzmann constant and M is the molar weight of CO_2 (in kg). Since the vibrational levels are treated as separate species, only the heat capacity due to translational and rotational degrees of freedom and, in the case of CO_2, also the heat capacity due to the symmetric vibrational modes, which are not treated as individual species, should be taken into account [10,11]. A classical partitioning between the translational and rotational degrees of

freedom is assumed, which gives a value for the specific heat ratio, at room temperature and above, of 1.67 for the atomic species and 1.40 for the diatomic molecules . For O_3, a value of 1.27 was taken [10,12]. Details about the calculation of the total heat capacity and the resulting specific heat ratio for CO_2, calculated using equation (10), can be found in [10].

Table S.1: Electron impact reactions calculated with cross sections data, using the calculated EEDF, as explained in section 2.1 of the main paper, as well as the references where the data are adopted from.

No.	Reaction	Ref	Note
$(X1)^a$	$e^- + \ CO_2 \rightarrow 2e^- + CO_2^+$	[13–15]	
$(X2)^a$	$e^- + \ CO_2 \rightarrow 2e^- + O + CO^+$	[13–15]	
$(X3)^a$	$e^- + \ CO_2 \rightarrow 2e^- + O^+ + CO$	[16]	
$(X4)^a$	$e^- + \ CO_2 \rightarrow 2e^- + O_2 + C^+$	[16]	
$(X5)^a$	$e^- + \ CO_2 \rightarrow 2e^- + O_2^+ + C$	[17]	
$(X6)^a$	$e^- + \ CO_2 \rightarrow O^- + CO$	[13–15]	
$(X7)^b$	$e^- + \ CO_2 \rightarrow e^- + O + CO$	[13–15]	
$(X8)^a$	$e^- + \ CO_2 \rightarrow e^- + CO_2(E1)$	[13–15]	
$(X9)^b$	$e^- + \ CO_2 \leftrightarrow e^- + CO_2(Vx)$	[13–15]	$x = a, b, c, d$
$(X10)^c$	$e^- + \ CO_2 \leftrightarrow e^- + CO_2(Vi)$	[13–15]	$i = 1 - 21$
$(X11)^a$	$e^- + \ CO \rightarrow 2e^- + CO^+$	[18]	
$(X12)^a$	$e^- + \ CO \rightarrow 2e^- + C^+ + O$	[19]	
$(X13)^a$	$e^- + \ CO \rightarrow 2e^- + C + O^+$	[19]	
$(X14)^a$	$e^- + \ CO \rightarrow C + O^-$	[20]	
$(X14bis)^b$	$e^- + \ CO \rightarrow e^- + C + O$	[21]	
$(X15)$	$e^- + \ CO \leftrightarrow e^- + CO(Vi)$	[21]	$i = 1 - 10$
$(X16)^b$	$e^- + \ O_2 \rightarrow e^- + O + O$	[22]	

$(X16M)^a$	$e^- + O_2 + M \rightarrow O_2^- + M$	[22]	
$(X17)^a$	$e^- + O_2 \rightarrow O + O^-$	[22]	
$(X18)^a$	$e^- + O_2 \rightarrow 2e^- + O_2^+$	[23]	
$(X19)^b$	$e^- + O_2 \rightarrow 2e^- + O + O^+$	[23]	
$(X20)$	$e^- + O_2 \leftrightarrow e^- + O_2(Vi)$	[22]	$i = 1,2,3,4$
$(X21)$	$e^- + O_3 \rightarrow e^- + O_2 + O$	[24]	
$(X22)$	$e^- + O_3 \rightarrow 2e^- + O_2^+ + O$	[24]	
$(X23)$	$e^- + O_3 \rightarrow e^- + O^+ + O^- + O$	[24]	
$(X24)$	$e^- + O_3 \rightarrow O^- + O_2$	[25]	
$(X25)$	$e^- + O_3 \rightarrow O + O_2^-$	[25]	
$(X26)$	$e^- + O \rightarrow 2e^- + O^+$	[26]	
$(X27)$	$e^- + C \rightarrow 2e^- + C^+$	[27]	

[a] Same cross section also used for ground state.

[b] Cross section also used for the excited states, modified by lowering the energy threshold by the energy of the excited state.

[c] Cross section for the various levels (i,j) adopted from $e^- + CO_2 \rightarrow e^- + CO_2(Vi)$ but scaled and shifted using Fridman's approximation [28,29]

Table S.2: Electron impact reactions using analytical expressions for the rate coefficients, given in $m^3\ s^{-1}$ and $m^6\ s^{-1}$, for two-body and three-body reactions, respectively, as well as the references where the data are adopted from. T_g and T_e are given in K and eV, respectively.

No.	Reaction	Rate coefficient	Ref
$(E1a)$	$e^- + CO_2^+ \rightarrow CO(V1) + O$	$1.0x10^{-11}T_e^{-0.5}T_g^{-1}$	[30,31]
$(E1b)$	$e^- + CO_2^+ \rightarrow C + O_2$	$1.0x10^{-11}T_e^{-0.5}T_g^{-1}$	[17]
$(E2)^a$	$e^- + CO_4^+ \rightarrow CO_2 + O_2$	$1.61x10^{-13}T_e^{-0.5}$	[17]

$(E3)$	$e^- + \ CO^+ \rightarrow C + O$	$3.46x10^{-14}T_e^{-0.48}$	[32,33]
$(E4)^a$	$e^- + \ O + M \rightarrow O^- + M$	$1.0x10^{-43}$	[31]
[a] The primary source was not accessible			

Table S.3: Ion-ion and ion-neutral reactions, as well as the references where the data are adopted from. The rate coefficients are given in $m^3\ s^{-1}$ and $m^6\ s^{-1}$, for two-body and three-body reactions, respectively. T_g is given in K.

No.	Reaction	Rate coefficient	Ref
$(I1)$	$CO_2 + CO^+ \rightarrow CO_2^+ + CO$	$1.0x10^{-15}$	[34,35]
$(I2)$	$CO_2 + O^- + M \rightarrow CO_3^- + M$	$1.5x10^{-40}$	[34,36]
$(I3)$	$CO_2 + O_2^- + M \rightarrow CO_4^- + M$	$4.7x10^{-41}$	[34,36]
$(I4)$	$CO + O^- \rightarrow CO_2 + e^-$	$5.5x10^{-16}$	[34,37]
$(I5)$	$CO + CO_3^- \rightarrow 2CO_2 + e^-$	$5.0x10^{-19}$	[38]
$(I6)^a$	$CO_3^- + CO_2^+ \rightarrow 2CO_2(Vb) + O$	$5.0x10^{-13}$	[31]
$(I7)^a$	$CO_4^- + CO_2^+ \rightarrow 2CO_2(Vb) + O_2$	$5.0x10^{-13}$	[31]
$(I8)^a$	$O_2^- + CO_2^+ \rightarrow CO_2(V1) + O_2 + O$	$6.0x10^{-13}$	[31]
$(I9)$	$CO_3^- + O \rightarrow CO_2 + O_2^-$	$8.0x10^{-17}$	[39]
$(I10a)^a$	$CO_4^- + O \rightarrow CO_3^- + O_2$	$1.12x10^{-16}$	[34]
$(I10b)^a$	$CO_4^- + O \rightarrow CO_2 + O_2 + O^-$	$1.4x10^{-17}$	[34]
$(I11)$	$O + O^- \rightarrow O_2 + e^-$	$2.3x10^{-16}$	[40]
$(I12)^a$	$O + O_2^- \rightarrow O_2 + O^-$	$1.5x10^{-16}$	[34]
$(I13)$	$O_2^- + M \rightarrow O_2 + M + e^-$	$2.7x10^{-16}(\frac{T_g}{300})^{0.5}\exp(-5590/T_g)$	[41,42]
$(I14)^c$	$O^- + M \rightarrow O + M + e^-$	$2.3x10^{-15}\exp(-26000/T_g)$	[42–44]

[a] The primary source was not accessible

[c] For usual values of gas temperature, i.e. T_g<< 26,000 K, the rate coefficient is very low, as pointed out by Gudmundsson[45].

Table S.4: : Neutral-neutral reactions, as well as the references where the data are adopted from. The rate coefficients are given in m^3 s^{-1} and m^6 s^{-1}, for two-body and three-body reactions, respectively. T_g is given in K. The α parameter determines the effectiveness of lowering the activation energy for reactions involving vibrationally excited levels of the molecules (see details in [28,29])

No.	Reaction	Rate coefficient	α	Ref
$(N1)$	$CO_2 + M \rightarrow CO + O + M$	$6.06x10^{-16}\exp(-52525/T_g)$	0.82	[46]
$(N2)$	$CO_2 + O \rightarrow CO + O_2$	$2.8x10^{-17}\exp(-26500/T_g)$	0.50	[47,48]
$(N3)$	$CO_2 + C \rightarrow 2CO$	$< 1.0x10^{-21}$	n.a.	[49]
$(N4)$	$CO + O + M \rightarrow CO_2 + M$	$8.3x10^{-46}\exp(-1510/T_g)$	0.0	[48,50]
$(N5)$	$O_2 + CO \rightarrow CO_2 + O$	$4.2x10^{-18}\exp(-24000/T_g)$	0.5	[48]
$(N6)$	$O_2 + C \rightarrow CO + O$	$1.99x10^{-16}\exp(-2010/T_g)$	0.0	[51]
$(N7)$	$O + C + M \rightarrow CO + M$	$2.14x10^{-41}\left(\frac{T_g}{300}\right)^{-3.08}\exp(-2144/T_g)$	0.0	[47,48]
$(N8)$	$O + O + M \rightarrow O_2 + M$	$5.2x10^{-47}\exp(900/T_g)$	n.a.	[47,48]
$(N9)$	$O_2 + M \rightarrow O + O + M$	$3.0x10^{-12}\frac{1}{T_g}\exp(-59380/T_g)$	1.0	[47,48]

Table S.5: Neutral reactions between vibrationally excited molecules, as well as the references where the data are adopted from. The rate coefficients are given in m^3 s^{-1} and m^6 s^{-1}, for two-body and three-body reactions, respectively. T_g is given in K.

No.	Reaction	Rate coefficient	Ref

$(V1)$	$CO_2(Va) + M \rightarrow CO_2 + M$	$7.14x10^{-15}\exp(-177T_g^{-1/3} + 451T_g^{-2/3})$	[52–54]
$(V2a)$	$CO_2(V1) + M \rightarrow CO_2(Va) + M$	$4.25x10^{-7}\exp(-407T_g^{-1/3} + 824T_g^{-2/3})$	[54–56]
$(V2b)$	$CO_2(V1) + M \rightarrow CO_2(Vb) + M$	$8.57x10^{-7}\exp(-404T_g^{-1/3} + 1096T_g^{-2/3})$	[54–56]
$(V2c)$	$CO_2(V1) + M \rightarrow CO_2(Vc) + M$	$1.43x10^{-7}\exp(-252T_g^{-1/3} + 685T_g^{-2/3})$	[54–56]
$(V3)$	$CO(V1) + M \rightarrow CO + M$	$1.0x10^{-18}T_g\exp(-150.7T_g^{-1/3})$	[57]
$(V4)$	$O_2(V1) + M \rightarrow O_2 + M$	$1.3x10^{-14}\exp(-158.7T_g^{-1/3})$	[53,54]
$(V5)$	$CO_2(V1) + CO_2 \rightarrow CO_2(Va) + CO_2(Vb)$	$1.06x10^{-11}\exp(-242T_g^{-1/3} + 633T_g^{-2/3})$	[54–56]
$(V6)$	$CO_2(V1) + CO_2 \rightarrow CO_2 + CO_2(V1)$	$1.32x10^{-18}\left(\frac{T_g}{300}\right)^{0.5}\frac{250}{T_g}$	[58,59]
$(V7)$	$CO(V1) + CO \rightarrow CO + CO(V1)$	$3.4x10^{-16}\left(\frac{T_g}{300}\right)^{0.5}(1.64x10^{-6}T_g + \frac{1.61}{T_g})$	[60,61]
$(V8)$	$CO_2(V1) + CO \rightarrow CO_2 + CO(V1)$	$4.8x10^{-12}\exp(-153T_g^{-1/3})$	[54,55]

2. Extra calculated plasma characteristics

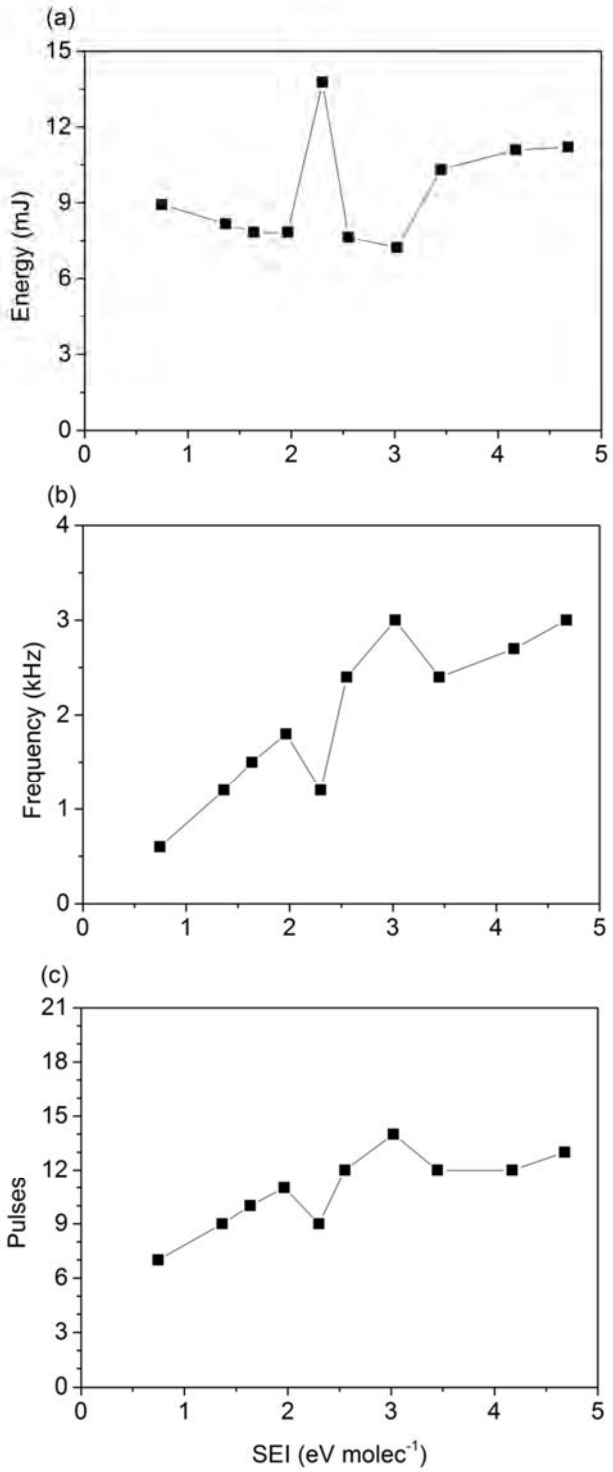

Figure S.1: Energy deposited per pulse (a), pulse frequency (b), and number of pulses felt by the gas molecules when travelling from pin HV electrode to grounded electrode (c), for the different SEI values investigated.

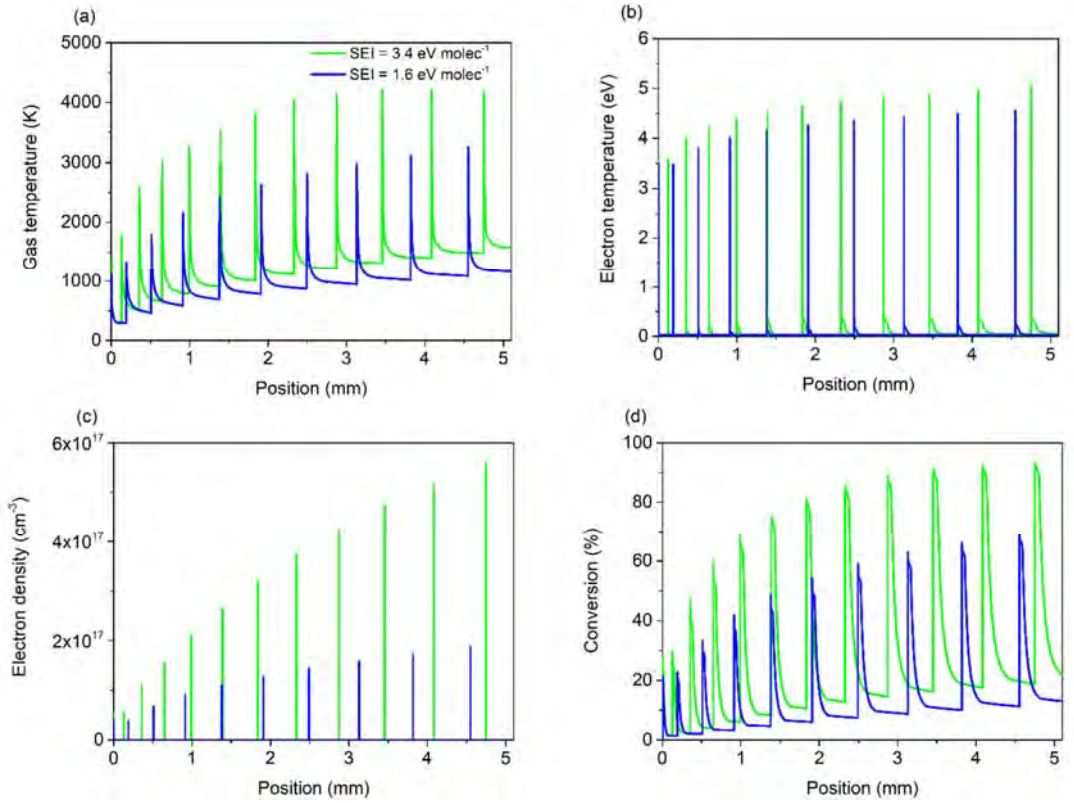

Figure S.2: Calculated gas temperature (a), electron temperature (b), electron density (c), and CO_2 conversion (d), as a function of travelled distance between HV pin electrode and grounded electrode, for two different SEI values (i.e. different from the SEI values in Figure 7 in the main paper, for extra information).

3. Details about the dissociation and formation mechanisms, and contribution of vibrational levels

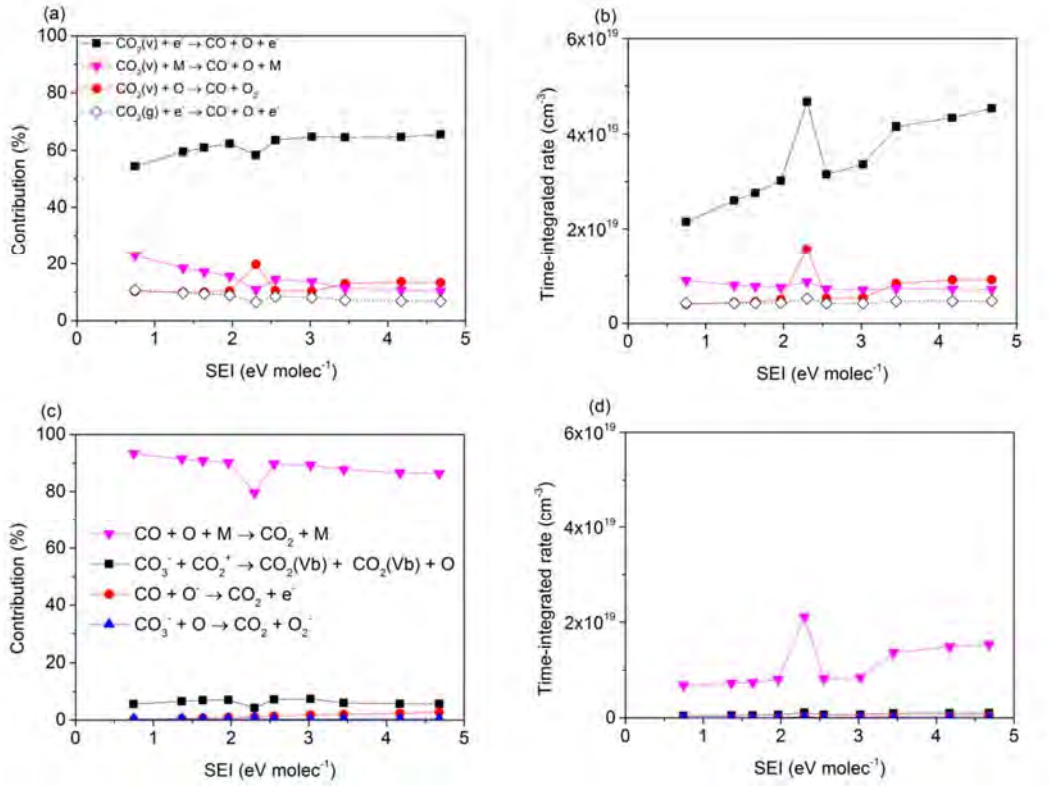

Figure S.3: Contribution of the most important dissociation (a) and formation (c) mechanisms of CO_2, and their corresponding time-integrated rates (b, d) as a function of SEI.

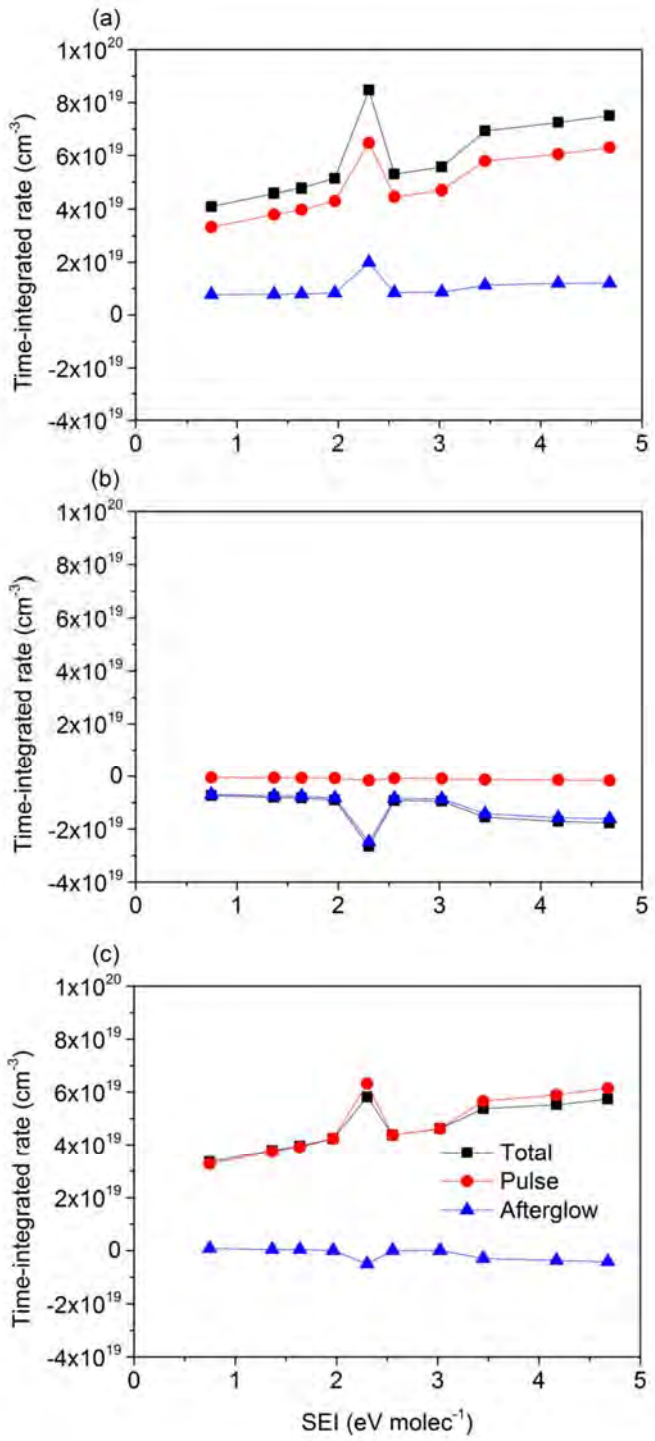

Figure S.4: Time-integrated rates of the overall dissociation (a), overall formation (plotted as negative values) (b), and the net dissociation of CO_2, as a function of SEI, for the pulse, afterglow and the sum of both (total), showing that the dissociation mainly takes place during the pulses, while net formation occurs during the afterglows.

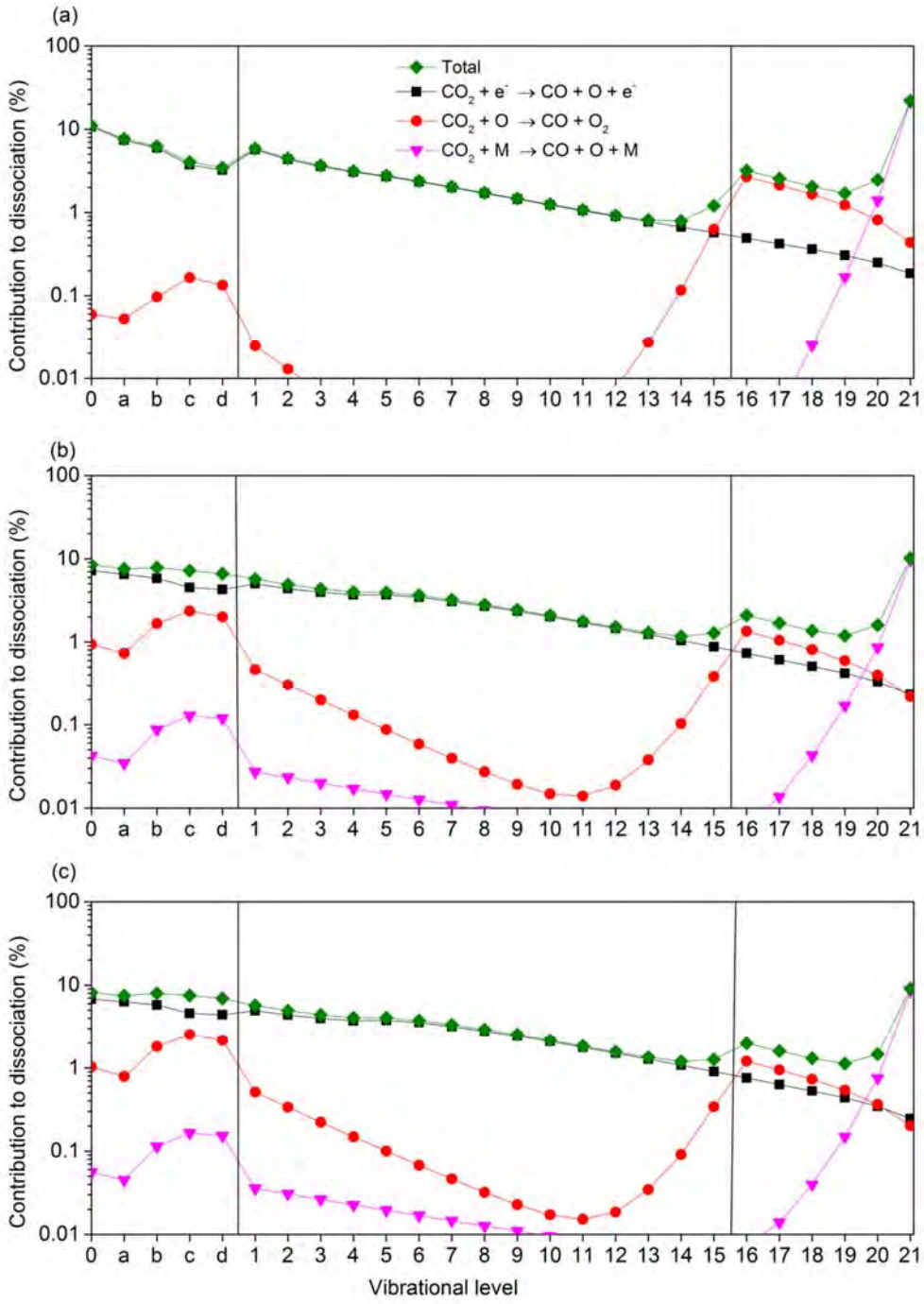

Figure S.5: Contribution of the CO_2 ground state and different vibrational levels to the total dissociation, as well as to the most important dissociation mechanisms, only accounting for the forward reactions, for different SEI values, i.e., 0.7 eV molec^{-1} (a), 3.4 eV molec^{-1} (b) and 4.7 eV molec^{-1} (c).

4. Details about the effect of cooling

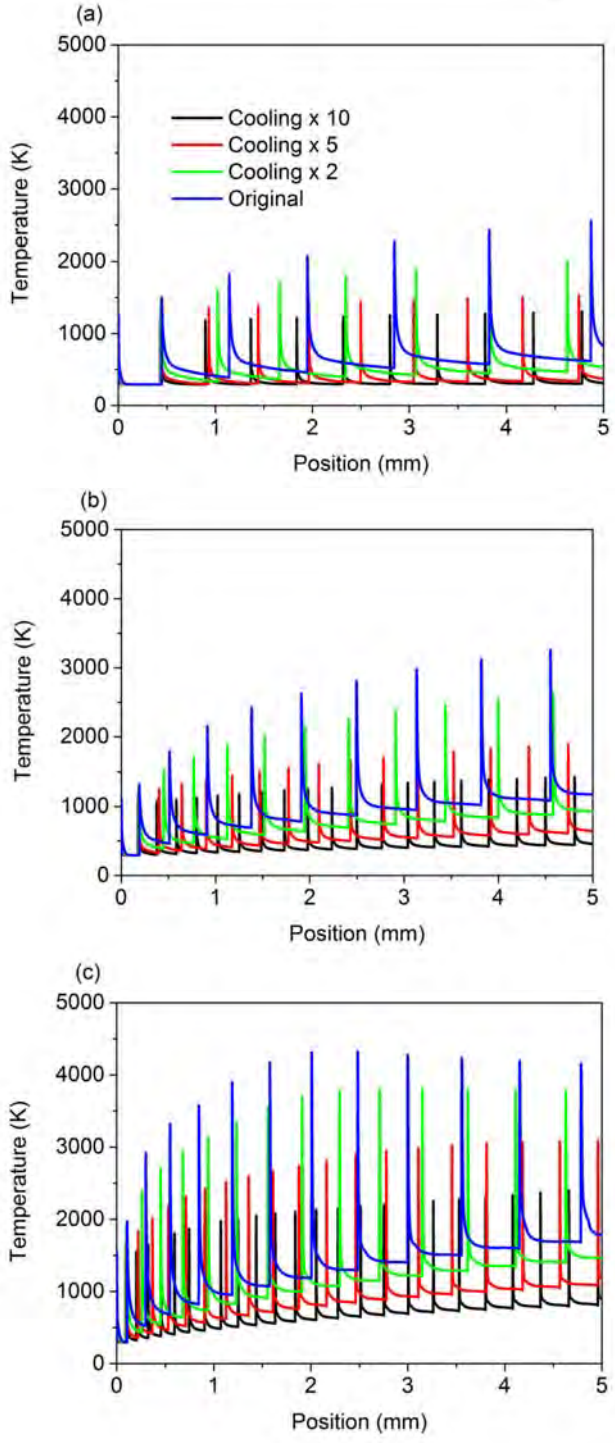

Figure S.6: Calculated gas temperature as a function of travelled distance between HV pin electrode and grounded electrode for different SEI values, i.e., 0.7 eV molec^{-1} (a), 1.6 eV molec^{-1} (b) and 4.7 eV molec^{-1} (c), at different cooling rates.

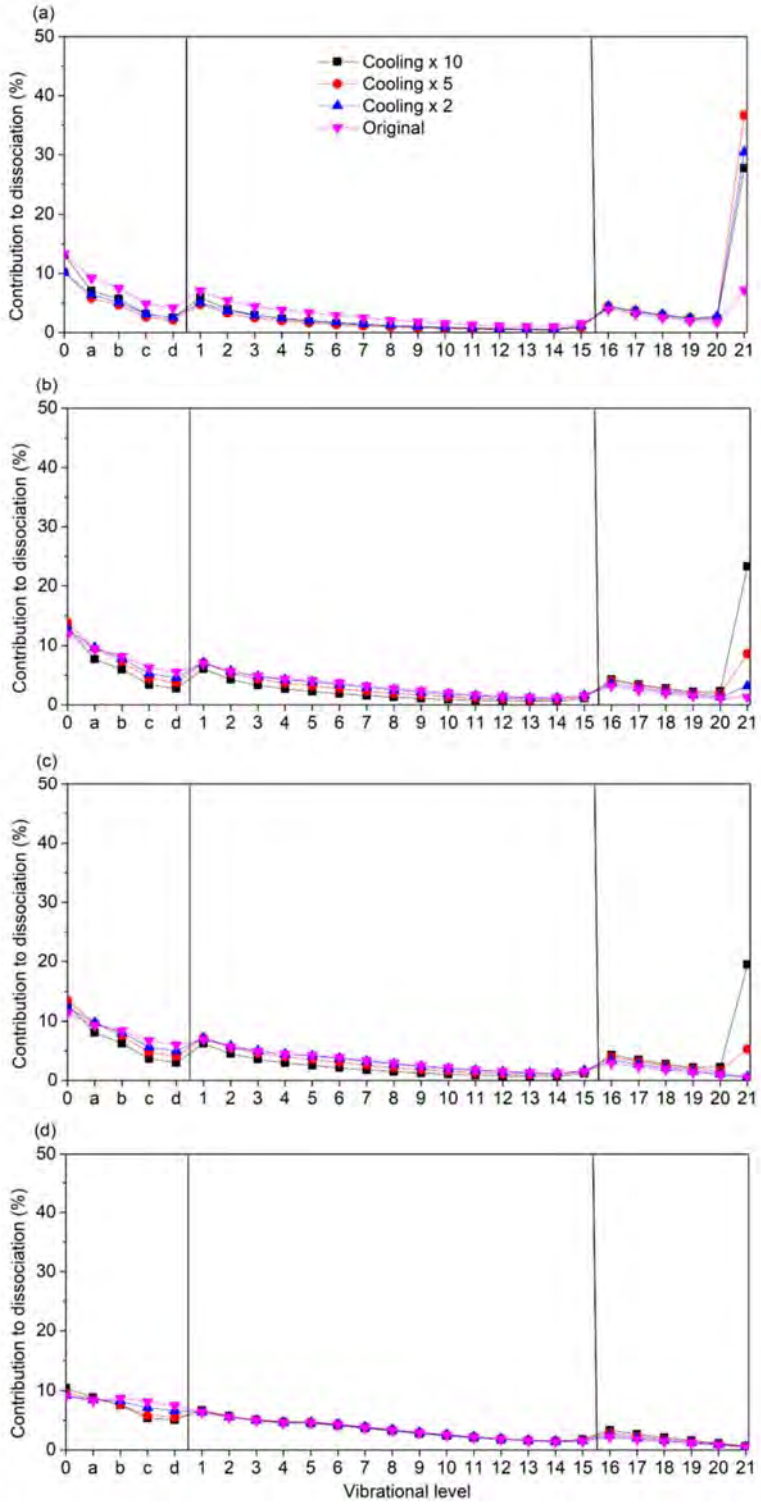

Figure S.7: Net contribution of the different CO_2 vibrational levels to the total dissociation, for different SEI values, i.e., 0.7 eV molec^{-1} (a), 1.6 eV molec^{-1} (b), 2.0 eV molec^{-1} (c) and 4.7 eV molec^{-1} (d), at different cooling rates.

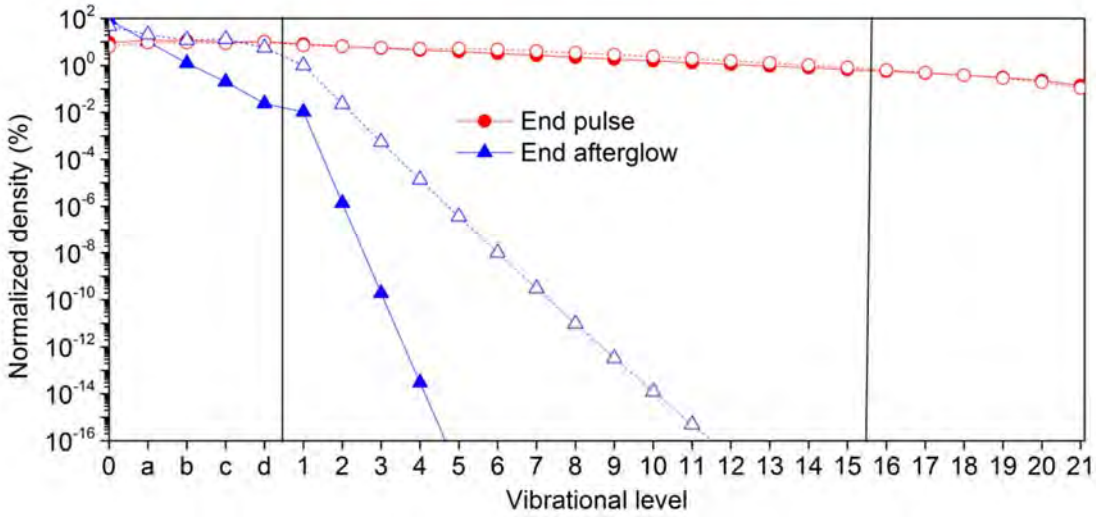

Figure S.8: Calculated VDFs at the end of the last pulse (10 ns) and at the end of the last afterglow, for SEI = 1.6 eV molec^{-1}, in the original model (open symbols, dashed lines) and with a cooling rate times ten (solid symbols and lines). The VDFs at cooling rate times two and five at the end of the pulse are the same, and at the end of the afterglow, they lie in between the VDFs of the original model and of ten times higher cooling rate.

5. References

(1) Pancheshnyi, S.; Eismann, B.; Hagelaar, G. J. M.; Pitchford, L. C. ZDPlasKin: A New Tool for Plasmachemical Simulations. University of Toulouse, LAPLACE, CNRS-UPS-INP, Toulouse, France, 2008, p University of Toulouse, LAPLACE, CNRS-UPS-INP.

(2) Hagelaar, G. J. M.; Pitchford, L. C. Solving the Boltzmann Equation to Obtain Electron Transport Coefficients and Rate Coefficients for Fluid Models. *Plasma Sources Sci. Technol.* **2005**, *14*, 722–733.

(3) Lieberman, M. A.; Lichtenberg, A. J. *Principles of Plasma Discharges and Materials Processing: Second Edition*, 2nd Editio.; Wiley-Interscience, 2005.

(4) Greig, J. R.; Pechacek, R. E.; Raleigh, M. Channel Cooling by Turbulent Convective Mixing. *Phys. Fluids* **1985**, *28*, 2357–2364.

(5) Shneider, M. N. Turbulent Decay of After-Spark Channels. *Phys. Plasmas* **2006**, *13*, 073501.

(6) Ramakers, M.; Trenchev, G.; Heijkers, S.; Wang, W.; Bogaerts, A. Gliding Arc Plasmatron: Providing a Novel Method for Carbon Dioxide Conversion. *Chem. Sus. Chem.* **2017**, *10*, 2642–2652.

(7) Cleiren, E.; Heijkers, S.; Ramakers, M.; Bogaerts, A. Dry Reforming of Methane in a Gliding Arc Plasmatron: Towards a Better Understanding of the Plasma Chemistry. *Chem. Sus. Chem.* **2017**, *10*, 4025–4036.

(8) Heijkers, S.; Bogaerts, A. CO_2 Conversion in a Gliding Arc Plasmatron: Elucidating the Chemistry through Kinetic Modeling. *J. Phys. Chem. C* **2017**, *121*, 22644–22655.

(9) Trenchev, G.; Kolev, S.; Wang, W.; Ramakers, M.; Bogaerts, A. CO_2 Conversion in a Gliding Arc Plasmatron: Multidimensional Modeling for Improved Efficiency. *J. Phys. Chem. C* **2017**, *121*, 24470–24479.

(10) Kozak, T.; Bogaerts, A. Evaluation of the Energy Efficiency of CO_2 Conversion in Microwave Discharges Using a Reaction Kinetics Model. *Plasma Sources Sci. Technol.* **2015**, *24*, 015024.

(11) Wang, W.; Berthelot, A.; Kolev, S.; Tu, X.; Bogaerts, A. CO_2 Conversion in a Gliding Arc Plasma: 1D Cylindrical Discharge Model. *Plasma Sources Sci. Technol.* **2016**, *25*, 065012.

(12) Chase, M. NIST-JANAF Thermochemical Tables, 4th Edition. *Journal of Physical and Chemical Reference Data, Monograph 9*. 1998, p 1952.

(13) Phelps, A. V. Phelps Database www.lxcat.net.

(14) Lowke, J. J.; Phelps, A. V.; Irwin, B. W. Predicted Electron Transport Coefficients and Operating Characteristics of CO_2/N_2/He Laser Mixtures. *J. Appl. Phys.* **1973**, *44*, 4664–4671.

(15) Hake, R. D.; Phelps, A. V. Momentum-Transfer and Inelastic-Collision Cross Sections for Electrons in O_2, CO, and CO_2. *Phys. Rev.* **1967**, *158*, 70–84.

(16) Itikawa, Y. Cross Sections for Electron Collisions with Carbon Dioxide. *J. Phys. Chem. Ref. Data* **2002**, *31*, 749–767.

(17) Beuthe, T. G.; Chang, J.-S. Chemical Kinetic Modelling of Non-Equilibrium Ar- CO_2 Thermal Plasmas. *Jpn. J. Appl. Phys.* **1997**, *36*, 4997–5002.

(18) Tian, C.; Vidal, C. R. Cross Sections of the Electron Impact Dissociative Ionization of CO, CH_4 and C_2H_2. *J. Phys. B At. Mol. Opt. Phys.* **1998**, *31*, 895–909.

(19) Itikawa, Y. Cross Sections for Electron Collisions with Carbon Monoxide. *J. Phys. Chem. Ref. Data* **2015**, *44*, 013105.

(20) Rapp, D.; Briglia, D. D. Total Cross Sections for Ionization and Attachment in Gases by Electron Impact. II. Negative-Ion Formation. *J. Chem. Phys.* **1965**, *43*, 1480–1489.

(21) Land, J. E. Electron Scattering Cross Sections for Momentum Transfer and Inelastic Excitation in Carbon Monoxide. *J. Appl. Phys.* **1978**, *49*, 5716–5721.

(22) Lawton, S. A.; Phelps, A. V. Excitation of the b 1Σ+g State of O_2 by Low Energy Electrons. *J. Chem. Phys.* **1978**, *69*, 1055–1068.

(23) Itikawa, Y. Cross Sections for Electron Collisions with Oxygen Molecules. *J. Phys. Chem. Ref. Data* **2009**, *38*, DOI: 10.1063/1.3025886.

(24) Eliasson, B.; Kogelschatz, U. *Basic Data for Modelling of Electrical Discharges in Gases: Oxygen*; Baden: ABB Asea Brown Boveri, 1986.

(25) Matejcik, S.; Kiendler, A.; Cicman, P.; Skalny, J.; Stampfli, P.; Illenberger, E.; Chu,

Y.; Stamatovic, A.; Märk, T. D. Electron Attachment to Molecules and Clusters of Atmospheric Relevance: Oxygen and Ozone. *Plasma Sources Sci. Technol.* **1997**, *6* (2), 140–146.

(26) Laher, R. R.; Gilmore, F. R. Updated Excitation and Ionization Cross Sections for Electron Impact on Atomic Oxygen. *J. Phys. Chem. Ref. Data* **1990**, *19*, 277–305.

(27) Morgan, W. L. Morgan Database Www.Lxcat.Net. *(retrieved 1 December 2015)*.

(28) Fridman, A. *Plasma Chemistry*; Cambridge University Press: New York, U.S.A., 2008.

(29) Kozák, T.; Bogaerts, A. Splitting of CO_2 by Vibrational Excitation in Non-Equilibrium Plasmas: A Reaction Kinetics Model. *Plasma Sources Sci. Technol.* **2014**, *23*, 045004.

(30) Weller, C. S.; Biondi, M. A. Measurements of Dissociative Recombination of CO_2^+ Ions with Electrons. *Phys. Rev. Lett.* **1967**, *19*, 59–61.

(31) Thoenes, J.; Kurzius, S. C. *Plasma Chemistry Processes in the Closed Cycle EDL-Technical Report DRCPMHEL-CR-79-11-VOL-1*; 1979.

(32) Mitchell, J. B. A.; Hus, H. The Dissociative Recombination and Excitation of CO+. *J. Phys. B At. Mol. Phys.* **1985**, *18*, 547–555.

(33) McElroy, D.; Walsh, C.; Markwick, A. J.; Cordiner, M. A.; Smith, K.; Millar, T. J. The UMIST Database for Astrochemistry 2012. *Astron. Astrophys.* **2012**, *550*, A36.

(34) Albritton, D. L. Ion-Neutral Reaction-Rate Constants Measured in Flow Reactors Through 1977. *At. Data Nucl. Data Tables* **1978**, *22*, 1–101.

(35) Adams, N. G.; Smith, D.; Grief, D. Reactions of H_nCO^+ Ions with Molecules at 300 K. *Int. J. Mass Spectrom. Ion Phys.* **1978**, *26*, 405–415.

(36) Fehsenfeld, F. C.; Ferguson, E. E. Laboratory Studies of Negative Ion Reactions with Atmospheric Trace Constituents. *J. Chem. Phys.* **1974**, *61*, 3181–3193.

(37) Mcfarland, M.; Albritton, D. L.; Fehsenfeld, F. C.; Ferguson, E. E.; Schmeltekopf, A. L. Flow-Drift Technique for Ion Mobility and Ion-Molecule Reaction Rate Constant Measurements. III. Negative Ion Reactions of O^- with CO, NO, H_2, and D_2. *J. Chem. Phys.* **1973**, *59*, 6629–6635.

(38) Price, D. A.; Moruzzi, J. L. Negative Ion Molecule Reactions in CO2 at High Pressures and Temperatures. *Vacuum* **1974**, *24*, 591–593.

(39) Fehsenfeld, F. C.; Schmeltekopf, A. L.; Schiff, H. I.; Ferguson, E. E. Laboratory Measurements of Negative Ion Reactions of Atmospheric Interest. *Planet. Space Sci.* **1967**, *15*, 373–379.

(40) Belostotsky, S. G.; Economou, D. J.; Lopaev, D. V.; Rakhimova, T. V. Negative Ion Destruction by $O(^3P)$ Atoms and $O_2(a\ ^1\Delta g)$ Molecules in an Oxygen Plasma. *Plasma Sources Sci. Technol.* **2005**, *14*, 532–542.

(41) Pack, J. L.; Phelps, A. V. Electron Attachment and Detachment. II. Mixtures of O_2 and CO_2 and of O_2 and H_2O. *J. Chem. Phys.* **1966**, *45*, 4316–4329.

(42) Bortner, M. H.; Bourer, T.; Blank, C. A. *Defense Nuclear Agency Reaction Rate*

Handbook, Second Edition AD 763699; 1972.

(43) Hasted, J. B.; Smith, R. A. The Detachment of Electrons from Negative Ions. *Proc. R. Soc. A Math. Phys. Eng. Sci.* **1956**, *235*, 349–353.

(44) Frommhold, L. Über Verzögerte Elektronen in Elektronenlawinen, Insbesondere in Sauerstoff Und Luft, Durch Bildung Und Zerfall Negativer Ionen (O-). *Fortschritte der Phys.* **1964**, *12*, 597–642.

(45) Gudmundsson, J. T. *A Critical Review of the Reaction Set for a Low Pressure Oxygen Processing Discharge RH-17-2004*; 2004.

(46) Burmeister, M.; Roth, P. ARAS Measurements on the Thermal Decomposition of CO_2. *AIAA J.* **1990**, *28*, 402–405.

(47) Baulch, D. L.; Drysdale, D. D.; Duxbury, J.; Grant, S. *Evaluated Kinetic Data for High Temperature Reactions, Volume 3: Homogeneous Gas Phase Reactions of the O_2-O_3 System, the CO-O_2-H_2 System, and of the Sulphur-Containing Species*; Butterworth, London, 1976.

(48) Tsang, W., R. F. H. Chemical Kinetic Data for Combustion Chemistry. Part 1. Methane and Related Compounds. *J. Phys. Chem. Ref. Data* **1986**, *15*, 1087–1279.

(49) Husain, D.; Young, A. N. Kinetic Investigation of Ground State Carbon Atoms, $C(2^3P_J)$. *J. Chem. Soc. Faraday Trans. 2* **1975**, *71*, 525.

(50) Baldwin, R. R.; Jackson, D.; Melvin, A.; Rossiter, B. N. The Second Limit of Hydrogen + Carbon Monoxide + Oxygen Mixtures. *Int. J. Chem. Kinet.* **1972**, *4*, 277–292.

(51) Dean, A. J.; Davidson, D. F.; Hanson, R. K. A Shock Tube Study of Reactions of C Atoms with H_2 and O_2 Using Excimer Photolysis of C_3O_2 and C Atom Atomic Resonance Absorption Spectroscopy. *J. Phys. Chem.* **1991**, *95*, 183–191.

(52) Simpson, C. J. S. M.; Chandler, T. R. D.; Strawson, A. C. Vibrational Relaxation in CO_2 and CO_2-Ar Mixtures Studied Using a Shock Tube and a Laser-Schlieren Technique. *J. Chem. Phys.* **1969**, *51*, 2214–2219.

(53) Taylor, R.; Bitterman, S. Survey of Vibrational Relaxation Data for Processes Important in the CO_2-N_2 Laser System. *Rev. Mod. Phys.* **1969**, *41*, 26–47.

(54) Blauer, J. A.; Nickerson, G. R. *A Survey of Vibrational Relaxation Rate Data For Processes Important To CO_2-N_2-H_2O Infrared Plume Radiation*; 1973.

(55) Rosser, W. A.; Wood, A. D.; Gerry, E. T. Deactivation of Vibrationally Excited Carbon Dioxide (v3) by Collisions with Carbon Dioxide or with Nitrogen. *J. Chem. Phys.* **1969**, *50*, 4996–5008.

(56) Herzfeld, K. F. Deactivation of Vibrations by Collision in the Presence of Fermi Resonance. *J. Chem. Phys.* **1967**, *47*, 743–752.

(57) Capitelli, M.; Ferreira, C. M.; Gordiets, B. F.; A.I., O. *Capitelli - Plasma Kinetics in Atmospheric Gases*; Springer(Berlin), 2000.

(58) Sharma, R. D. Near-Resonant Vibrational Energy Transfer Among Isotopes of CO_2.

Phys. Rev. **1969**, *177*, 102–107.

(59) Kreutz, T. G.; O'Neill, J. A.; Flynn, G. W. Diode Laser Absorption Probe of Vibration-Vibration Energy Transfer in CO_2. *J. Phys. Chem.* **1987**, *91*, 5540–5543.

(60) DeLeon, R. L.; Rich, J. W. Vibrational Energy Exchange Rates in Carbon Monoxide. *Chem. Phys.* **1986**, *107*, 283–292.

(61) Flament, C.; George, T.; Meister, K. A.; Tufts, J. C.; Rich, J. W.; Subramaniam, V. V.; Martin, J. P.; Piar, B.; Perrin, M. Y. Nonequilibrium Vibrational Kinetics of Carbon Monoxide at High Translational Mode Temperatures. *Chem. Phys.* **1992**, *163*, 241–262.